D~~Introducing d~~rone-based GPR application to~~in~~ snow hydrology ~~studies~~

Eole Valence[1,2], Michel Baraer[1,2], Eric Rosa[2,3], Florent Barbecot[2,4], Chloe Monty[1]

[1]Hydrology, Climate and Change (HC^3) Laboratory~~[1]Departement de genie de la construction~~, Ecole de Technologie Superieure, Montreal, H3C 1K3, Canada
[2]Geotop, Montreal, H2X 3Y7, Canada
[3]Groupe de recherche sur l'eau souterraine, Universite du Quebec en Abitibi-Temiscamingue, Rouyn-Noranda, J9X 5E4, Canada
[4]Departement des sciences de la Terre et de l'atmosphere, Universite du Quebec a Montreal, Montreal, H2L 2C4, Canada

Correspondence to: Eole Valence (eole.valence.1@ens.etsmtl.ca)

a mis en forme : Anglais (Royaume-Uni)

Abstract.

Seasonal snowpack deeply influences the distribution of meltwater among watercourses and groundwater. During rain-on-snow (ROS) events, the structure and properties of the different snow and ice layers dictate the quantity and timing of water flowing out of the snowpack, increasing the risk of flooding and ice jams. With ongoing climate change, a better understanding of the processes and internal properties influencing snowpack outflows is needed to predict the hydrological consequences of winter melting episodes and increases in the frequency of ROS events. This study develops a multi-method approach to monitor the key snowpack properties in a non-mountainous environment in a repeated and non-destructive way. Snowpack evolution during the winter of 2020–2021 was evaluated using a drone-based, ground-penetrating radar (GPR) coupled with photogrammetry surveys conducted at the Sainte-Marthe experimental watershed in Quebec, Canada. Drone-based surveys were performed over a 200 m^2 area with a flat and a sloped section. In addition, time domain reflectometry (TDR) measurements were used to follow water flow through the snowpack and identify drivers of the changes in snowpack conditions, as observed in the drone-based surveys.

The experimental watershed is equipped with state-of-the-art automatic weather stations that, together with weekly snow pit measurements over the ablation period, served as a reference for the multi-method monitoring approach. Drone surveys conducted on a weekly basis were used to generate georeferenced snow depth, density, snow water equivalent and bulk liquid water content maps.

Despite some limitations, the results show that the combination of drone based GPR, photogrammetric surveys and TDR is very promising for assessing the spatiotemporal evolution of the key hydrological characteristics of the snowpack. For instance, the tested method allowed for measuring marked differences in snow pack behaviour between the first and second weeks of the ablation period. A ROS event that occurred during the first week did not generate significant changes in snow pack density, liquid water content and water equivalent, while another one that happened in the second week of ablation generated changes in all three variables. After the second week of ablation, differences in density, LWC and SWE between the flat and the sloped sections of the study area were detected by the drone-based GPR measurements. Comparison between different events was made possible by the contact-free nature of the drone-based measurements.

~~Seasonal snowpack deeply influences the distribution of meltwater among watercourses and groundwater. During rain-on-snow (ROS) events, for instance, the structure and properties of the different ice and snow layers dictate the quantity of water flowing out of the snowpack, increasing the risk of flooding and ice jams. With ongoing climate change, a better understanding of the processes and internal properties influencing snowpack outflows is needed to predict the hydrological consequences as mild episodes and ROS events' frequency increases. This study aims to develop a multi-method approach to monitor the key snowpack properties in a non-mountainous environment in a repetitive and non-destructive way. Snowpack evolution was evaluated using a combination of drone-based GPR, photogrammetry surveys and time domain reflectometry (TDR) measurements, tested during the winter of 2020–2021 at the Sainte-Marthe experimental watershed, Quebec, Canada.~~

~~The experimental watershed is equipped with state-of-the-art automatic weather stations that, together with weekly snow pit measurements, serve as a reference for the multi-method monitoring approach. Drone surveys conducted on a weekly basis are used to generate georeferenced snow depth, relative density, snow water equivalent and average liquid water content maps. In between site visits, snowpack properties are monitored using TDR probes.~~

~~Despite some limitations, the results show that the approach is very promising in assessing the spatiotemporal evolution of the key hydrological characteristics of the snowpack. Among others, results showed the prevalence of preferential pathways at the early stage of the ablation period, the difference in hydrological reaction to a ROS event between flat and sloped sections of the study area and the hydrological influence of solar radiation at the late stage of the ablation period.~~

1 Introduction

By acting as transient storage, seasonal snow cover determines the amplitude of spring floods, the level of late summer flows and the recharge of aquifers (Dewalle and Rango, 2008). Snowmelt floods are a cause of economic losses and sometimes loss of life (Ding et al., 2021), while insufficient aquifer recharge affects water availability for agricultural and industrial uses, fresh water supply and the ecology of river systems (Dierauer, Allen et al. 2021).

Recent changes in snow cover characteristics have been reported from different regions of the globe (Magnusson, Jonas et al. 2010, Zhang, Yao et al. 2015), (Hodgkins and Dudley 2006, Cho, McCrary et al. 2021, Ford, Kendall et al. 2021) (Najafi, Zwiers et al. 2017). Climate change projections anticipate further alteration of snowpack characteristics: seasonal snowpack depth is expected to diminish (Dierauer, Allen et al. 2021), the winter maximum snow water equivalent to decline (Sun, Berg et al. 2019) and the spring melt to occur earlier in the season (Gergel, Nijssen et al. 2017). Moreover, observations and models indicate an increase in the number of winter rain-on-snow (ROS) events (Li, Lettenmaier et al. 2019). Combined with changes in snowpack characteristics, those events are predicted to trigger increases in winter flood and ice jam intensity and frequency (Morse and Turcotte 2018, Andradóttir, Arnardóttir et al. 2021).

Within this context, monitoring the spatiotemporal evolution of snow cover properties appears essential for anticipating adverse climate change consequences on winter hydrology and groundwater recharge (Lindström, Pers et al. 2010).

Snow depth (*h*), snow water equivalent (*SWE*), density (*ρ*), and liquid water content (*LWC*) are among the most measured properties of the snowpack (Kinar and Pomeroy 2015). These four variables are considered key properties for characterizing the snowpack's hydrological behaviour (Vionnet, Mortimer et al. 2021). Different technics have been developed over time to independently monitor those four variables over very limited surfaces (less than 100 m^2 for most of them):

- Snow depth is widely monitored using ultrasonic sensors (Doesken, Ryan et al. 2008), and methods like global navigation satellite system interferometric reflectometry (GNSS-IR) (Chen, Li et al. 2021) and terrestrial laser scanning (Prokop 2008, Revuelto, López-Moreno et al. 2015, Deems, Painter et al. 2017) are gaining in popularity. Still, destructive manual measurements remain extensively used for snow depth surveying (Leppänen, Kontu et al. 2016).
- *SWE* can be calculated based on manual snow-coring to estimate sample volume and mass. The manual method is time-consuming, destructive and of moderate precision (Goodison, Glynn et al. 1987, Morris and Cooper 2003, Sturm and Holmgren 2018, Paquotte and Baraer 2022). Automatic monitoring makes it possible to capture *SWE* temporal variability. The methods most often used are gamma ray monitoring (GMON), cosmic ray neutron probe (CNRP), snow pillows and plates, the system for acoustic sensing of snow (SAS2), the snowpack analyzer (SPA-2) and GNSS receiver-based SWE estimators (Yu, Li et al. 2020). Most of those technics require site calibration.
- Snow density is commonly measured through gravimetric measurements or calculated from snow depth and *SWE* measurements (Conger and McClung 2009). In dry conditions, snow density can be estimated with a dielectric permittivity measurement system such as the Finnish SnowFork (Hao, Mind'je et al. 2021). Other methods include neutron probes (Hawley, Brandt et al. 2008) and diffuse near-infrared transmission (Gergely, Schneebeli et al. 2010).
- The most common in situ *LWC* measurement methods are based on snow permittivity measurements. The SnowFork (Sihvola and Tiuri 1986), the Denoth device (Denoth 1995) and the A2 Photonic WISe sensor (Webb, Marziliano et al. 2021) are among the most popular devices to measure *LWC*. They all have an accuracy level of around 1% of the volumetric *LWC*. The most accurate method, however, which is often used as a reference for those devices, is freezing or melting calorimetry (Mavrovic, Madore et al. 2020, Webb, Marziliano et al. 2021). *LWC* may be monitored unattended using time domain reflectometry (TDR), but multiday monitoring using that technique still presents a challenge (Lundberg, Gustafsson et al. 2016).

Even if they are accurate in following the evolution of each variable in time, those techniques do not allow for capturing the spatial variability in the snowpack properties unless they are repeated at a multitude of points. Remote sensing represents an attractive alternative for that purpose.

With a vertical accuracy of less than 10 centimetres, airborne photogrammetry allows for a non-destructive monitoring of the spatial variability of snow depth in open areas (Bühler, Adams et al. 2016, Avanzi, Bianchi et al. 2018, Harder, Pomeroy et al.

2020, Jacobs, Hunsaker et al. 2021). In forested areas, airborne lidar (light detection and ranging) has proven a more accurate option (Koutantou, Mazzotti et al. 2021, Dharmadasa, Kinnard et al. 2022). The use of satellite-based remote sensing for *snow depth* and, by extension, *SWE* mapping has received much attention over the past decade (Guneriussen, Høgda et al. 2001, Rott, Nagler et al. 2003). While showing promising results and fast improvements in large open areas of several square kilometres range (e.g. McGrath, Webb et al. 2019), satellite-based *SWE* and/or snow depth estimations still involves coarse spatial data with a high degree of uncertainty when passive sensors are used (Mortimer, Mudryk et al. 2020), and some accuracy challenges still exist with active sensors (Pfaffhuber, Lieser et al. 2017). This is the case in mountainous areas, for example (Dai and Che 2022).

From the 1980s onward, the use of ground-penetrating radar (GPR) has been seen as a solution to overcome the difficulties in capturing key properties of and spatial variability in the snow pack, as described above (Marchand, Killingtveit et al. 2003). First carried by the operator, GPR airborne and ground-vehicle-based applications have risen in popularity due to their abilities to cover transects that are one tenth of a kilometre long (Sand and Bruland 1998). Radargrams generated using GPR show the influence a milieu has on the emitted electromagnetic wave that travels through it. This influence is characterized by the milieu's permittivity, expressed as a complex number. For snow layers, the real component of the permittivity is mostly a function of snow density, snow depth and *LWC*. As *SWE* can be calculated from snow depth and density, GPR therefore allows for measuring a physical characteristic that is related to the four key snowpack properties in a single survey (Di Paolo, Cosciotti et al. 2020).

Since the '80s, GPR has been shown to be a valuable tool for measuring physical snowpack characteristics (Holbrook, Miller et al. 2016). It is one of the most-used methods in snowpack studies (Vergnano, Franco et al. 2022), and the spatial variability of snow properties has been extensively assessed using GPR (Lundberg, Granlund et al. 2010, Previati, Godio et al. 2011, Holbrook, Miller et al. 2016).

However, GPR applications in monitoring one or several of the four key snowpack characteristics still involve different challenges, such as that:

1. The real component of the permittivity requires the snow depth to be known or estimated (Di Paolo, Cosciotti et al. 2020).
2. Different empirical equations have been developed to relate snow density and *LWC* to the real component of the permittivity (Frolov and Macheret 1999, Di Paolo, Cosciotti et al. 2018). In dry conditions, *LWC* being neglectable, a direct relation exists between the snow density and the relative permittivity. On the other hand, the introduction of liquid water into the snowpack cannot be accurately characterized with GPR velocity alone (Bradford and Harper 2018). In absence of other measurements allowing for mapping of *LWC* or snow density in wet conditions, either an assumption need to be made regarding snow density variability from spot measurements (e.g., Webb, Wigmore et al. 2020; Yildiz, Akyurek et al. 2021) or an empirical relation must be parametrized by calibration (e.g. Singh, Negi et al. 2017).

3. Ground-based GPR applications requires direct contact with the snow surface, modifying its properties (Valence and Baraer, 2021) and making subsequent surveys not fully representative of natural conditions.
4. Air surveys such as the helicopter-based ones are limited by high operating costs, while ground-based surveys are difficult to conduct on unstable and steep slopes (Vergnano, Franco et al. 2022).

Recent developments show interesting potential to overcome those challenges. Combining GPR applications with other measurements has been shown to be a howevern efficient way to overcome the two first challenges. For instance, Marchuk and Grigoryevsky (2021) improved GPR-based snow depth profiling by associating GPR to a laser range finder. The use of drone-based surface mapping methods such as photogrammetry or lidar in snowpack studies is provides reliable snow depth maps (Bühler, Stoffel et al. 2016). Lundberg, Gustafsson et al. (2016) and Yildiz, Akyurek et al. (2021) used drone-based photogrammetry or lidar to integrate snow depth measurements into *SWE* calculations. Combining techniques that monitor the temporal evolution of the snow permittivity, such as TDR, with GPR has been shown to be a promising approach to studying snowpack spatial variability over a given period (Godio, Frigo et al. 2018). Estimating *LWC* from frequency-dependent attenuation of the GPR signal, as proposed by Bradford, Harper et al. (2009) is another way to address the wet snowpack characterization issues.

Actual developments in drone-borne GPR have opened new avenues in GPR-based snowpack studies (Francke and Dobrovolskiy 2021). Recent studies have shown it to be valuable in snow avalanche applications (McCormack and Vaa 2019) and in snow depth mapping (Tan, Eccleston et al. 2018, Vergnano, Franco et al. 2022). Similarly, drone-based ultra-wide-band (Jenssen and Jacobsen 2022) and software-defined radar (Prager et al. 2022) applications to snowpack characterization surveys have recently been demonstrated to be potentially ground-breaking solutions.

The present study aimed to tentatively monitor the spatiotemporal variability in snow depth, snow density, *SWE* and snow *LWC* of a snowpack over flat and sloped areas with a non-destructive approach. This objective was achieved by combining some of the emerging solutions described above with more traditional snow-monitoring techniques in a novel way. This combination included drone-based photogrammetry; drone-based GPR; and continuous monitoring of *SWE*, snow depth and snow permittivity using TDR and snow pit-based measurements.

~~The seasonal snow cover is of great hydrological influence in cold regions. By acting as seasonal transient storage, it determines the amplitude of spring floods, the level of late summer flows and the recharge of aquifers (Dewalle and Rango, 2008). Snowmelt floods are a cause of economic losses and sometimes loss of life (Ding et al., 2021), while insufficient aquifer recharge impacts water availability for agricultural and industrial uses, fresh water supply and the ecology of river systems (Dierauer et al., 2021).~~

~~Economic sectors, such as hydroelectric power (Brown et al., 2018), and agriculture (Liu and Lobb, 2021) show high vulnerability to changes in the snow cover and related hydrological impacts. Changes in snow cover characteristics have been reported from different regions of the Globe. For example, a decline in snow-covered area has been observed over the Tibetan~~

~~plateau (Zhang et al., 2015), along with losses in snowpack water storage in Europe (Magnusson et al., 2010), densification of snowpack in eastern North America (Hodgkins and Dudley, 2006; Ford et al., 2021; Cho et al., 2021) and decline of spring snow cover in western Canada (Najafi et al., 2017). Climate change projections anticipate further alteration of snowpack characteristics. Due to climate change, seasonal snowpack depth is expected to diminish (Dierauer et al., 2021), the winter maximum snow water equivalent to decline (Sun et al., 2019) and the spring melt to occur earlier in the season (Gergel et al., 2017).~~

~~Moreover, observations and models indicate an increase in the number of rain-on-snow (ROS) events during the winter from 1950 to 2013 (Li et al., 2019). Combined with changes in snowpack characteristics, those events are predicted to trigger an increase in winter flood and ice jam intensity and frequency (Morse and Turcotte, 2018; Andradóttir et al., 2021).~~

~~Snowpack physical characteristics and hydrological behavior are deeply interrelated (Mas et al., 2018). While the snowpack structure controls internal water fluxes, liquid water movement, storage and phase change in the snowpack transform and modify that structure (Quéno et al., 2020). Within this context, monitoring the spatiotemporal evolution of snow cover properties appears essential for anticipating adverse climate change consequences on winter hydrology and groundwater recharge (Lindström et al., 2010).~~

~~Snow depth (h), density (ρ), snow water equivalent (SWE) and liquid water content (LWC) are among the most measured physical quantities of the snowpack (Kinar and Pomeroy, 2015a). These four variables are considered as key properties for characterizing the snowpack's hydrological behavior (Vionnet et al., 2021) and show high variability in time and in space, making them difficult to capture at the appropriate scale.~~

~~Snow depth is widely monitored using ultrasonic sensors, with an accuracy of 2 cm (Doesken et al., 2008). More recently, h measurements using Global Navigation Satellite System Interferometric Reflectometry (GNSS-IR) have grown in popularity (Chen et al., 2021). Terrestrial laser scanning has been successfully used for h distributed measurements with a vertical accuracy of 10 cm (Prokop, 2008; Revuelto et al., 2015; Deems et al., 2017). Airborne photogrammetry shows great potential for h measurement. With a centimeter scale accuracy, this technique allows for the non-destructive monitoring of the spatial variability of h (Bühler et al., 2016a; Avanzi et al., 2018). However, airborne photogrammetry application is limited to open environments (Harder et al., 2020; Jacobs et al., 2021). By contrast, airborne lidar (light detection and ranging) h measurements have proven to be efficient in forest environments (Koutantou et al., 2021). Even with growing access to those remote measurement techniques, destructive manual measurements remain extensively used for snow monitoring (Leppänen et al., 2016).~~

~~Indeed, h measurement using rods and rules is still seen as a reference to capture h spatial variability and/or to validate remote sensing measurements (Kinar and Pomeroy, 2015b).~~

~~Snow density is commonly measured through gravimetric measurements or calculated from h and SWE measurements (Conger and Mcclung, 2009). In dry conditions, snow density can be estimated with a dielectric permittivity measurement systems such as the Finnish SnowFork (Hao et al., 2021). Other methods include time domain reflectometry (TDR), ground-penetrating~~

~~radar measurement (Previati et al., 2011; Holbrook et al., 2016), neutron probe (Hawley et al., 2008) and diffuse near-infrared transmission (Gergely et al., 2010).~~

~~Different methods are used to measure the spatial variation of *SWE*. Manual measurements consist of snow-coring to estimate sample volume and mass. The manual method is time-consuming, destructive, and of moderate precision {Sturm, 2018 #55;Beaudoin-Galaise, 2021 #272}. Where hard layers are present, sequential sampling is required, making the method more labor intensive (Morris and Cooper, 2003; Paquotte and Baraer, 2022). Manual methods are subject to operational sampling errors and bias (Goodison et al., 1987). Automatic monitoring makes it possible to capture *SWE* variability temporally. The methods most often used are gamma ray monitoring (GMON), cosmic ray neutron probe (CNRP), snow pillows and plates, the system for acoustic sensing of snow (SAS2) and the snowpack analyzer (SPA-2). GMON and CNRP require site calibration, and the stationary version of SAS2 has a limited footprint (2–3 m of diameter) (Kinar and Pomeroy, 2015a; Royer et al., 2021). Moreover, the high price of automatic monitoring systems limit their large-scale deployment. Snow pillows and plates are limited to flat areas, while freeze and thaw events may affect their functioning. GNSS receiver-based *SWE* estimations are an emerging alternative to the above-mentioned automatic measurement systems. However, they still require calibration using a reference method (Yu et al., 2020). The use of satellite-based remote sensing for *SWE* measurement has received much attention over the past decade(Dietz et al., 2012). For example, repetitive L-band measurements allow the InSAR applications to map *SWE* over large areas (Rott et al., 2003; Guneriussen et al., 2001). However, the method still needs some improvements for application in wooded areas. Passive microwave remote sensing provides information over large areas on snow mass, which can be related to *SWE* (Foster et al., 2005). Thus, it provides coarse spatial data with a high degree of uncertainty (Mortimer et al., 2020).~~

~~The most common in situ *LWC* measurement methods are based on snow dielectric constant measurements at single points of the snowpack. The SnowFork (Sihvola and Tiuri, 1986), the Denoth device (Denoth, 1995) and the A2 Photonic WISe sensor (Webb et al., 2021) are among the most popular devices to measure *LWC*. They all present an accuracy of around 1% of the volumetric *LWC*. The most accurate method, often used as a reference for those devices is freezing or melting calorimetry (Mavrovic et al., 2020; Webb et al., 2021). *LWC* may be monitored with radar (Lundberg et al., 2013), TDR (Lundberg et al., 2016) or devices such as SAS2 and SPA-2.~~

~~So far, taken individually none of the methods presented here above can capture the spatiotemporal variability of the snowpack's hydrological behavior at representative scales.~~

~~Combining techniques that monitor the temporal evolution of the snow permittivity at a sub-hourly time step such as TDR, with those mapping its variation in space such as GPR is therefore seen as a promising approach to address this challenge (Godio et al., 2018). Different empirical fuctions have been developed to relate ρ and *LWC* to the measured permittivity (Di Paolo et al., 2018; Frolov and Macheret, 1999). In dry conditions, *LWC* can be neglected, leaving a direct relation between ρ and the relative permittivity. In wet conditions, either assumptions are made on ρ variability from spot measurements (e.g., Webb et al. (2020); Yildiz et al. (2021)) or ρ maps must be produced using a separate method. In that regard, the *LWC* estimation from frequency-dependent attenuation of the GPR signal proposed by (Bradford et al., 2009) shows great potential.~~

~~As *SWE* can be calculated from ρ and *h*, measuring *h* from methods such as drone-based photogrammetry or lidar can provide more direct and precise *SWE* estimation (Lundberg et al., 2016).~~

~~One of the main drawbacks of using GPR over the snowpack is the required contact between the GPR carrier and the snow, which affects snowpack integrity, makes subsequent surveys not fully representative of natural conditions. Recently developed drone-based systems provides non-invasive and large-scale monitoring of snow cover properties (Bühler et al., 2016b). To our knowledge, there has been very little research to date using drone-based radar measurement for snow property monitoring {Jenssen, 2020 #43;Prager, 2022 #140;Vergnano, 2022 #273}.~~

~~The present study aims to monitor the spatiotemporal variability in *h*, ρ, *SWE* and *LWC* of a snowpack over flat and sloped area with a non-destructive approach. This objective is achieved by developing and testing an original combination of drone-based photogrammetry, drone-based GPR and continuous automatic monitoring including TDR, and field measurements.~~

2 Study site ~~and condition~~

The study was conducted at the BVE Ste-Marthe, an experimental watershed located approximately 70 km west of Montréal, in Quebec, Canada (45.4239°N, 74.2840°W) (Fig. 1a.). ~~The study region is the experimental watershed (BVE) of Ste-Marthe, located approximately 70 km west of Montréal, in Quebec, Canada (45.4239°N, 74.2840°W) (Figure 1.a).~~ The main station of the BVE Ste-Marthe is situated at 120 m above sea level~~.a.s.l~~. in an approximately 200 m^2 large forest clearing (Fig. 1~~.~~b. and Fig. 1c.). A distinction is made between two different topographic~~y~~ areas of the clearing~~ance~~, one of approximately 30 m^2 categorized as flat and the other of approximately 50 m^2 categorized as sloped (Fig. 1d.~~10%~~). In addition, t~~T~~he ~~main station hosts an~~ automatic weather station (AWS) ~~that~~ measures various hydroclimatic variables listed in Table 1. ~~All data were recorded using a CR1000 data logger (Campbell Scientific). Monitored variables used for the purpose of this study are presented in Table 1. The snowpack outflow at the snow/ground interface was measured thanks to a custom-built 2.25 m^2 snow lysimeter.~~

~~The frozen ground depth was estimated by interpolation of ground temperatures measured at thermometers buried in the ground from -10 to -60 cm at 10 cm depth intervals. To avoid interpreting snowpack temperature data that could have been influenced by solar radiation or by contact with air, snowpack temperature measurements are not considered after March 17, 2021, the day the snow height decreased below 40 cm.~~

Measurements took place during the winter of 2020-21, from February 26 to March 26. ~~Measurements used in this study took place during winter, from February 26, 2021 to March 26, 2021.~~ Two rain-on-snow (ROS) events occurred during this period. The first ROS was observed from February 28 to March 1, and the second from March 9 to 12.

Four drone-based surveys and snow pits were made during the~~at~~ ablation period on February 26, March 5, March 12 and March 19.

Field visits for drone-based surveys and snow pit measurements occurred on February 26, March 5, March 12 and March 19. February 26 corresponded to the onset of the accumulation period, while the ablation period started February 27.

~~Figure 2 presents the AWS measurements of interest over the study period. February 26 is considered as the last survey before the end of the accumulation period, just before the day of maximum snow depth of the winter (February 27).~~

3 Methods

The spatiotemporal variability of snow depth~~h~~, snow density~~ρ~~, *SWE* and snow *LWC* was assessed by combining different methods with different sampling approaches. Table 2 provides an overview of the different methods used. They are split into three categories, depending on the frequency of measurements and the spatial coverage. ~~Repetitive~~Repeated surveys conducted on the two different areas are used to produce maps of the four studied variables on a weekly basis. Continuous and ~~repetitive~~repeated measurements at a single point are used as comparison~~a reference to evaluate~~ to the maps ~~accuracy~~ data at a given point of the study area. TDR probes represent an exception to that rule. A total of eight probes were split between two areas~~spots~~, one within the flat area and the second within the sloped area. At each spot, probes were placed on different hard layers on the snowpack. These layers were identified as possible vectors for lateral flow (Evans et al., 2016).

3.1 AWS monitoring

Data from the AWS were recorded using a Campbell Scientific CR1000 data logger. AWS sensors included the snow lysimeter situated at less than 10 m from the surveyed flat area, and presented a comparable exposition to sunlight. Therefore, it was expected that both snow depth records would exhibit comparable results. The snow's relative density was calculated using the snow depth and the SWE measurements, following equation 1:

$$SWE = h.\rho\,, \qquad (1)$$

SWE and h are both in metres, and ρ is dimensionless.

The frozen ground depth was estimated by interpolation of ground temperatures measured from 10 to 60 cm below the ground level at 10 cm depth intervals. Snowpack temperature was measured with four thermometers at 0, 10, 20 and 30 cm above the ground level. To avoid using snowpack temperature measurements that could have been influenced by solar radiation or by contact with air, snowpack temperature measurements were not considered after March 17, 2021, the day the snow height decreased below 40 cm above ground level.

~~All data were recorded using a CR1000 data logger (Campbell Scientific). Monitored variables used for the purpose of this study are presented in Table 1. The snowpack outflow at the snow/ground interface was measured thanks to a custom-built 2.25 m^2 snow lysimeter.~~

~~The frozen ground depth was estimated by interpolation of ground temperatures measured at thermometers buried in the ground from -10 to -60 cm at 10 cm depth intervals. To avoid interpreting snowpack temperature data that could have been influenced by solar radiation or by contact with air, snowpack temperature measurements are not considered after March 17, 2021, the day the snow height decreased below 40 cm.~~

3.2~~1~~ Manual measurements

Manual measurements were proceeded on a weekly basis, the same days as the drone surveys. Snow pits were excavated north oriented at approximately 75 cm from the last one ~~in the flat area~~ following the method presented by Fierz et al. (2009). The snow pits were located at less than 3m from the flat area used for the drone-based measurements and presented a comparable exposition to ~~For~~sunlight. For each pit, layer identification was followed by a sequential depth, density and snow temperature measurements. Each layer was isolated from the preceding layer using a thin metallic plate and sampled using a metallic cylinder of 0.3 dm^2 or a cylindrical plastic sampler with a surface of 0.5 dm^2. The sample mass was measured in situ with a precision scale of ±1 g.

~~Punctual~~ *LWC* measurements were made in snow pit using an A2 Photonic WISe Sensor ~~(A2) at the snow pit~~. Two vertical measurement profiles with 10 cm intervals between observations were created for each snow pit. Even if the manufacturer's device precision is ±1% of *LWC*, we anticipate a higher uncertainty, as measurement through ice layers was not possible.

~~Manual measurements were used to estimate the bulk properties of the snowpack~~Snow pack total depth and~~. B~~bulk snow depth~~h~~ and *SWE* were just calculated by summing the individual layer ones. Bulk relative density~~ρ~~ and *LWC* were calculated by taking the weighted mean of the measurements based on layers' thickness~~length~~.

3.~~2~~3 TDR monitoring

The CS610 probes were controlled using a TDR200 (both from Campbell Scientific). Each probe was calibrated according to the Campbell Scientific guidelines in the laboratory before deployment. Onsite, each CS610 was inserted into the snow,~~left~~ lying over a hard layer without any guide or support. This setup was chosen to allow the probe to move downward together with the supporting hard layer as the snowpack settled. Indeed, maintaining probes at the exact same position above the ground triggers air pocket formation around the metallic rod, affecting the measurements' accuracy (Pérez Díaz et al., 2017). As no visible differences in stratigraphy were observed between the flat and sloped areas over the accumulation period, hard layers supporting the probes were identified the same way:

- α represents the ground level. Probes were installed January 8 in the flat area and January 26 at the base of the slope. At both locations, the snow layer on top of the ground was unconsolidated and heterogeneous.
- β is a wind crust formed December 30–31. Probes were installed the same days as on layer α. The layer β was overlaid by unconsolidated granular snow.
- γ is a hard settled snow layer ~~formed in mild~~ formed ~~conditions~~ on January 15. Probes were installed January 26. At that time, the hard snow layer was overlaid by a thin layer of fresh snow.
- ε is an ice layer formed during a freezing rain event that occurred February 16. Probes were installed on top of that layer on February 22 in both locations.

TDR probes measured the relative permittivity of the surrounding material. In snow, the relative permittivity is a function of the density and the liquid water content (Stacheder et al., 2009). Placed at different spots, initial relative permittivity values measured by the probes naturally differ slightly from each other. In order to allow comparison of the permittivity evolution between two probes placed over the same layer, relative permittivity values were normalized by dividing all values measured by a TDR probe by the first measurements made after installation of that given probe. value. Doing so allowed the researchers to start each TDR-derived time series from 1. With a 15-minute measurement interval, it was assumed that any sensible variations in permittivity (higher than 10% of the initial value) between two successive measurements was due to changes in liquid water content, as such changes would occur over a longer time scale if due to a change in snowpack density only (Stacheder et al., 2005).

~~With a 15-minute measurement interval, it was assumed that noticeable variations in permittivity between two measurements were due to changes in liquid water content, and that changes in density occurred over a longer timescale{Stacheder, 2005 #271}.~~

3.4~~3~~ Drone-based photogrammetry

A DJI Mavic 2 Pro drone was used to capture the RGB images used for photogrammetry. During a flight time of approximately 20 minutes, the drone took around 200 images with an 80% overlap at an elevation of 25 m above ground level. The Mavic 2 Pro is equipped with a TopoDrone global navigation satellite system (GNSS) to allow post-processing kinematic (PPK) treatment to correct images' locations. The uncertainty claimed by the manufacturer is 3–5 cm in all directions. PPK corrections were made using a Reach RS2 GNSS base station, with a manufacturer's uncertainty of 4 mm in the horizontal direction and 8 mm in the vertical. After each site visit, collected images were processed using the Pix4Dmapper software to produce digital surface models (DSMs). The expected horizontal resolution is 0.6 cm per pixel. Vertical accuracy was assessed using ground control points (GCP). For each survey, ten GCP were disposed all around the study area; GCP were placed approximately at the same position for each survey. Control points were geo-localized using a KlauGeomatic 7700B GNSS rover, ensuring a 5-cm accuracy. Comparing the uncorrected DSM models produced by photogrammetry to the DSM models after correction using control points showed variations under 3 cm in all three directions, which is within the expected accuracy of the Klau GNSS. The use of control points did not lead to meaningful improvements of the map georeferencing, validating the accuracy of maps produced using PPK adjustments only.

Finally, snow depth maps were produced by subtracting a snow-free DSM produced on April 6, just after the complete thaw of the snow cover and just before the vegetation growth, from the DSM produced in winter conditions. This was done using the ESRI Geographic Information System (GIS) software ArcGIS, following the protocol presented by Bühler et al. (2016) and Yildiz et al. (2021).

~~A Mavic 2 Pro UAV (DJI) was used to capture the RGB images used for photogrammetry. The Mavic 2 Pro was upgraded using a global navigation satellite system (GNSS) kit (TopoDrone) to use Post Processed Kinematic (PPK) to correct images' location. The uncertainty claimed by the manufacturer is 3–5 cm in all directions. Corrections were made using a RS2 (Reach)~~

~~GNSS base station, with a manufacturer's uncertainty of 4 mm in the horizontal direction and 8 mm in the vertical. After each site visit, collected images were processed using the photogrammetry software Pix4Dmapper (Pix4D) to produce digital surface models (DSMs). Ground control points, geo-localized using a 7700B GNSS rover (KlauGeomatic), were used for DSM validation and provide a 3–5 cm uncertainty.~~ ~~The final error of the drone photogrammetry is estimated at ±5 cm.~~~~Finally, validated DSMs were evaluated and quantified using the Geographic Information System (GIS) software ArcGIS (ESRI). Following the protocol presented by Bühler et al. (2016a) and used by Yildiz et al. (2021), the GIS data was used to subtract a snow-free DSM produced on April 6, just after the complete thaw of the snow cover, from the DSM made using images taken over the winter.~~ ~~The final error of the drone photogrammetry is estimated at ±5 cm.~~

3.54 Drone-based GPR permittivity measurement

GPR surveys were performed using a Radar System Inc. Zond 1.5 GHz ~~(Radar System Inc.)~~ carried by a DJI Matrice (M) 600 Pro drone ~~(DJI)~~. GPR integration and the flight control software (UGCS) were supplied by SPH Engineering. Maximizing GPR measurements requires flying at 1.2 m/s and at approximately~~-~~ 1 m above the surveyed surface, managed using a terrain-following system also supplied by SPH Engineering. The UgCS SkyHub on-board computer maintain the altitude above the snow surface using data from an on-board altimeter. In addition, this on-board computer allows the alimentation and the setting for GPR. The M600 was equipped with a KlauGeomatic 7700B GNSS ~~(KlauGeomatic)~~ allowing position correction via ~~Post Processed Kinematic (~~PPK~~)~~. Similar to the photogrammetry, PPK corrections were made using the Reach RS2 ~~(Reach)~~ GNSS as a base station. Therefore, GPR data were referenced by post treatment with the KlauGeomatic PPK solution. Surveys were performed over both the flat and sloped areas. Radargrams' post-treatment was made with the Radar System Inc. Prism2 software ~~(Radar System Inc.)~~. The GPR system was sampled every 512 ns over both flat and sloped areas, and the drone's flight following north-south transects. Thus, the spatial resolution of GPR measurements is function of the actual drone speed (different from expected drone speed due to wind and other meteorological conditions affecting the drone flight) and the sampling frequency. For each survey, six transects on the flat area and nine transects on the slope were surveyed. The distance between two consecutive transects was 50 ± 2~~1~~0 cm. Post-treatment consisted of applying a background removal filter, adjusting the gain, and applying a time delay compensation. The ground/snow and snow/air interfaces were detected automatically wherever possible and manually where the layer boundaries were not recognized by the automatic graphic interpretation tool provided in Prism2 was not able to follow the layer boundaries over the transect~~algorithm~~. Example of two radargrams after processing layer boundaries tracking is presented Figure 3. Given that GPR measurements were geolocalized using PPK, t~~T~~he ~~overall uncertainty for~~ radargram georeferencing is considered to have a ~~be~~ 5 cm accuracy~~the same as for photogrammetry~~.

Snow depth for each GPR transect was extracted software from the snow depth maps produced by photogrammetry, using ArcGIS to guarantee data superposition. The velocity of the electromagnet~~n~~ic wave within the snowpack (v) and the snow height (h) extracted from the DSM are related as follows:

$$v = \frac{h}{TWT/2}, \qquad (2~~1~~)$$

where *TWT* is the two-way travel time of the wave within the snowpack in ns. *TWT* is extracted from the radargrams by taking the difference between the air/snow interface and snow/ground interface two-way travel times.

The relative permittivity of the snowpack is a complex number. Its real part (ε_s') is calculated using Neal (2004)

$$\varepsilon_s' = \left(\cancel{\frac{v}{\epsilon}}c/v\right)^2, \qquad (3~~2~~)$$

where *c* stands for the velocity of light in a vacuum (taken as equal to 0.3 m/ns).

3.6~~5~~ Drone-based GPR frequency-dependent attenuation analysis

In wet conditions, the imaginary part of the permittivity of the snow (ε_s'') is estimated using the GPR frequency-dependent attenuation analysis method proposed by Bradford et al. (2009). In the standard GPR frequency range (10 MHz–1 GHz), ε_s'' is strongly dependent on *LWC* and assumed to be independent of frequency. Assuming that the frequency-dependent attenuation of an electromagnetic wave through water is linearly related to frequency (Turner and Siggins, 1994), the attenuation coefficient over the GPR signal band can be written as

$$\alpha = \alpha_0 + \frac{\sqrt{\mu_0 \varepsilon_s'}}{2Q^*}\omega, \qquad (4~~3~~)$$

Where Q^* represents~~ing~~ the generalization of the attenuation quality parameter in the linear region of the attenuation, α_0 the impact of low frequencies in the radar attenuation, ω is the angular frequency and μ_0 the permeability in the free space. Within the frequency range of 1 to 1500 MHz, Q^* is assumed to be constant (Bradford et al., 2009) and related to ε_s'' as follows:

$$Q^* = \frac{\varepsilon_s'}{2\varepsilon_s''}, \qquad (5~~4~~)$$

Where a GPR generates waves in the form of a Ricker wavelet, the frequency f_0 of the spectral maximum of the GPR wave measured at the snow/air interface on the radargram and the frequency f_t of the spectral maximum measured at the ground/snow interface are related to Q^* (Bradford, 2007):

$$\begin{cases} \frac{1}{Q^*} = \frac{4}{TWT}\frac{\omega_0^2-\omega_t^2}{\omega_0^2\omega_t} \\ \omega_0 = 2\pi f_0 \\ \omega_t = 2\pi f_t \end{cases}, \qquad (6~~5~~)$$

In the present study, f_0 and f_t were measured by randomly sampling at least 10 points for each GPR line. For each selected point, readings were made on five consecutive traces using the Prism2 software. Peak frequencies for each point were calculated by taking the median of the measurements. When at least one trace showed a higher frequency at the ground/snow interface than at the snow/air interface, two extra traces were used; ε_s'' was then computed using equations (5~~4~~) and (6~~5~~), with ε_s' being calculated using equations (2) and (3~~2~~).

LWC and the relative density of dry snow (ρ_d) were then calculated with the following set of dimensionless empirical equations proposed by Tiuri et al. (1984) and Sihvola and Tiuri (1986):

$$\varepsilon_d' = (1 + 1.7\rho_d + 0.7\rho_d^2)\ , \tag{7~~6~~}$$

$$\varepsilon_s' = (0.1LWC + 0.8LWC)\varepsilon_w' + \varepsilon_d', \tag{8~~7~~}$$

$$\varepsilon_s'' = (0.1LWC + 0.8LWC)\varepsilon_w''\ , \tag{~~8~~9}$$

where ε_d' is the bulk permittivity of dry snow and ε_w' and ε_w'' are respectively the real and the imaginary parts of the relative permittivity of pure water.

Equations (7)~~2.6~~, (8)~~2.7~~, and (9)~~2.8~~ were established for a measurement frequency of 1 GHz and are assumed to remain valid for the purpose of the present study.

The relative snow density (ρ) is then calculated with the following dimensionless equation:

$$\rho\ = \rho_d + LWC, \tag{10~~9~~}$$

Finally, the *SWE* is calculated using the relative density (ρ) calculated with equation (10) and with the snow depth (h) extracted from the DSM produced by photogrammetry with equation (1).~~:~~

~~$SWE = h.\rho\ ,$~~ ~~(10)~~

LWC maps were then produced by extrapolating the punctual results to areas value using an inverse distance weighting ~~Kernel~~ interpolation with barriers set at 2 m. For each *LWC* maps, 10 ± 2 points per transects were randomly selected for the interpolation, the inverse distance exponent of distance used was set at 2, where the maximum distance for data calculation was set at 2 m, and the minimum number of points considered in the calculation was set at 3. The interpolation was used to create *LWC* maps of 5 cm cell size for each survey.~~algorithm with the Geostatistical Wizard module of the ArcGIS software.~~

For the surveys on February 26 and March 5, the snowpack was assumed to be dry, as the survey was preceded by several cold days with a snowpack temperature below 0°C. The *SWE* was determined using the assumptions that $\varepsilon_d'=\varepsilon_s'$, $\rho_s=\rho_d$, and $LWC=0$.

For the surveys on March 12 and March 19, the *SWE* was determined following the GPR attenuation analysis.

4 Results

4.1 AWS

Figure 3 presents the AWS relevant measurements over the study period. February 27 measured snowpack temperatures were all below 0°C and had not been altered by any significant ROS or major melt event yet.

Between February 27 and March 1, the snowpack was affected by a first mild episode (M.E.1) that ended with a ROS event. Mild episodes are here defined as more than 24-hour-long periods with continuous above-zero air temperatures. The first week of investigation was also characterized by several snow precipitation events. The ROS event lasted 45 minutes, with 1.6 mm of cumulative precipitations during the first 30 minutes and only 0.1 mm in the last 15 minutes. M.E. 1 warmed up the snowpack to nearly 0°C at all measured depths, generated slightly more than 1 mm of cumulative outflow at the base of the snowpack, and increased both the *SWE* and relative snow density to 15 mm equivalent and 0.05 mm, respectively. Outflow at the snowpack's base started while the measured snowpack temperatures were still negative, suggesting that at least part of the outflow was made of liquid precipitation flowing through the snowpack. M.E. 1 was followed by a drop in air temperature of 25 degrees C, starting the beginning of a seven-day-long cold period. Over that cold period, the measured snowpack temperatures dropped below 0°C, while *SWE* and relative snow density stabilized. Outflow at the snowpack's base stopped 24 hours after the temperature started to decrease. Considering that during this mild episode at least part of the ground remained frozen, with negative temperatures observed between 0 and -30 cm under the soil surface, it is assumed that no significant ground infiltration occurred during M.E. 1 (Dingman, 1975). This suggests that most of the rain percolation either froze inside the snowpack or flowed longitudinally at its base.

The second survey occurred March 5, during the seven-day-long cold period described here above, over a dry snowpack.

A second mild episode (M.E. 2), started on March 8 and lasting more than three days of almost M.E. 2, ended March 12, the day of the third survey. On March 11, the air temperature reached a maximum of 15°C and a ROS event occurred. It took two days for the warm conditions to warm the snowpack up to 0°C at all measurement points and to generate outflow at the snowpack's base. The second ROS event occurred on an already warm snowpack and produced 0.8 mm of precipitation over 30 minutes. This ROS event was therefore slightly less intense than the first one. The snow lysimeter measured a cumulative outflow comparable as during M.E. 1. As the soil remained frozen during this second mild episode, most of the water coming from the melt and from the precipitation was expected to have flowed horizontally at the base of the snowpack.

March 12 marked the last day of M.E. 2 with air temperatures falling under 0°C. Between March 8 and March 12, snow depth decreased by almost 30%, while *SWE* remained almost unchanged, despite substantial liquid precipitations being recorded. Snowpack temperatures and outflow measurements indicated that at least some of the snowpack layers were wet at the time of the survey. From March 12, air temperatures remained negative until March 17. A refreezing front slowly moved down the snowpack, and the outflows stopped over that period, suggesting a gradual drying of the snowpack. From March 17 to 18, a third mild episode (M.E. 3) brought the snowpack temperatures back to the melting point. An outflow of minor amplitude compared to those observed during the two first mild episodes was measured on March 18 only.

During the March 19 survey, the air temperature reached a maximum of -2°C. At that date, the snowpack was drying, with an almost continuous increase of snow density and a decreasing snowpack depth. These reached 0.48 and 38 cm, respectively. ~~On that date, the snowpack was cold (at least between 0 and +30 cm) and had not been affected by any significant ROS or major melt event yet.~~

~~Between February 27 and March 5, the date of the second survey, the snowpack was first affected by a mild weather episode of more than 24 hours ending with a ROS event. This episode warmed up the snowpack to nearly 0°C at all measured depths, generated a substantial outflow at the base of the snowpack and increased both the *SWE* and ρ. Interestingly, the outflow at the snowpack's base occurred while the measured snowpack temperatures were still negative, suggesting the presence of a preferential flow paths over the flat area. The mild weather episode was followed by a marked drop in air temperature, marking the start of a seven-day-long cold period. Over this cold period the snowpack temperatures dropped below 0°C, while *SWE* and ρ stabilized. Outflow at the snowpack's base stopped 24 hours after the temperature decreased.~~

~~Prior to the third survey on March 12, there was a four-day long episode of almost uninterrupted above 0°C air temperatures. On March 11 the air temperature reached a maximum of 15°C and a ROS event occurred. It took two days for the warm conditions to warm the snowpack up to 0°C and to generate outflow at the snowpack's base. The timing and amplitude of the outflow suggest a more homogeneous flow path was present at the time.~~

~~March 12 marked the last day of the second mild episode. Snow depth decreased by almost 30%, while *SWE* remained almost unchanged since the last survey, despite substantial liquid precipitations being recorded. Snowpack temperatures and outflow indicate that at least some of the snowpack layers were wet at the time of the survey. At the end of March 12, the air temperature gradually decreased below zero. From that time, air temperatures remained negative until March 17. A freezing front slowly moved down the snowpack, and an interruption of the outflows was observed over that period, suggesting a gradual drying of the snow layers. From March 17 to 19, the dominant warm conditions brought the snowpack temperatures back to the melting point. An outflow of minor amplitude compared to those observed during the two first warm episodes was measured only on March 18. On the March 19 survey, the air temperature dropped down to -2°C.~~

~~After March 19, a strong diurnal signal in the outflow marks the start of an uninterrupted loss of mass from the snowpack. Note that over the studied period, at least part of the ground remained frozen, creating a quasi-impermeable barrier to water infiltration (Dingman, 1975).~~

4.2~~1~~ Drone-based photogrammetry

Snow cover maps produced using drone-based photogrammetry are presented in Figure 4. On top of the uncertainty estimation described above, the maps are fully consistent with field observations. The quality of the DSM allows for identifying specific features such as trails used to access different features of the study area (e.g., lines in yellow on the 2020-02-26 map). Those trails show lower than pristine snow depths in a consistent way. Similarly, extra snow accumulation in drainage ditches (e.g., brown area in the bottom left area of the 2020-03-19 map) is well marked and consistently apparent on the different sub-figures). Overall, the snow depth maps are considered to have satisfactory accuracy for the purpose of the study.

By comparing the different Figure 4 maps, we can observe that the snow depth decrease that occurred between February 26 and March 5 is homogeneous over the entire area, with no differences between the flat and sloped areas being visually noticeable. Snow depth in both areas on February 26 ranged between 60 cm and 90 cm, while on March 5, the snow depth ranged from 50 cm to 80 cm in both slope and flat areas. The situation is different when comparing the March 12 map to these two first dates. On March 12, flat area snow depth ranged from 35 cm to 55 cm, whereas the slope area snow depth was between 25 cm and 50 cm. The severe ablation and/or settling that affected the study area impacted the sloped area more than the flat one. Changes in snow depth were less pronounced between March 12 and 19 than for the previous periods. Maximum snow depth in the flat area decreased from 55 to 50 cm, and from 50 to 45 cm in the sloped area between March 12 and 19. Between March 5 and March 12, the maximum snow depth in the flat area decreased by 25 cm and by 30 cm in the sloped area.

Overall, Figure 4 shows that the sloped and flat sections had comparable snow depths at the end of the accumulation period but reacted differently to ablation, with a faster loss of depth in the sloped area than in the flat one.

~~None of the control points used in each survey showed significant difference with the PPK-based DSM produced by photogrammetry, validating the method for the purpose of this study. Further, the adjustments made at the final stage of the DSM production, when ground control points were compared with PPK-based points, were all under 3 cm, which is within the expected accuracy of the PPK devices.~~

~~Maps of snow depth obtained from the photogrammetry are presented in Figure 3.~~

~~The individual maps make visually accurate representations of the study site. Prints of the paths we used over the entire season (e.g., lines in yellow on the 26/02 map) show consistent reductions in snow depth compared to pristine areas. Similarly, extra snow accumulation in drainage ditches (e.g., brown area in the bottom left area of the 19/03 map) is well marked and consistent between the survey dates. Overall, those maps are considered as satisfactory for the purpose of the study.~~

~~By comparing the different survey dates, we observe that the snow depth decrease that occurred between February 26 and March 5 appears to be homogeneous over the entire area, with no differences between the flat and sloped areas being visually noticeable. This is not the case when comparing the March 12 map to the two first dates. The severe ablation and/or settling that affected the study area impacted the sloped area more than the flat one. Changes in snow depth were less pronounced between March 12 and 19 than for the previous period. However, the difference between the flat and sloped areas remained important.~~

~~Overall, Figure 3 shows that the sloped and flat sections had comparable snow depths during the accumulation period but reacted differently at the start of the ablation period, with a faster loss of height in the sloped area than in the flat one.~~

4.3~~2~~ TDR monitoring

Relative permittivity measured using TDR probes and normalized to the value measured on February 26 at 12:30 are presented in Figure 5. As described in the Methods section, rapid variations in relative permittivity are associated with a change in *LWC*. Given that an increase of more than 0.1 in normalized permittivity in 15 minutes can be considered as due to a change in *LWC*, the normalized relative permittivity is here used to assess the snowpack response to mild episodes in terms of water content and flow-through dynamics.

- M.E. 1. The first reaction to the M.E. 1 in terms of *LWC* was observed on top of the layer ε (Figure 5a). That increase in LWC led to an increase in normalized relative permittivity of 0.2 on February 27, the day after M.E. 1 began. Snowpack response to the February 28 ROS event occurred first at the bottom of the sloped area, as suggested by the increase of 1.2 of normalized relative permittivity over the α slope layer (Figure 4d). followed by an increase of 0.2 measured by the other TRD sensors. The detection of an increase in *LWC* at the base of the flat area occurred half a day after the increase for the sloped area, with an increase of about 0.7 of the normalized permittivity above both flat and slope α layers, at a time when the air temperature had already dropped below zero. Interestingly, the lysimeter measured an outflow at the base of the snowpack in the flat area 24 hours before any moisture increase was detected by the TDR probe placed on the ground in the flat area. Differences observed in timing and amplitudes at the different probe locations suggest that liquid water flows followed preferential pathways. Past that time, normalized permittivity steadily decreased in all spots, reaching a plateau representative of the new dry densities of the snow layers. The relative permittivity of the new plateau was10% higher than on February 26, suggesting a slight increase in density.
-
- M.E. 2. As was the case at the M.E. 1, the increase in normalizer relative permittivity was first observed at the base of the sloped area. The increase was followed by an increase at the other probes 24 hours later, those above the β and γ layers being of very low amplitude: 0.1 to 0.2 of normalized permittivity. The strongest increase in *LWC* was measured over the sloped ground layer (Figure 4d), with a normalized relative permittivity 4 times higher than the one measured February 26. At the end of March 10, three of the four probed layers showed an increase in *LWC*, which was more pronounced in the sloped area than in the flat area. After March 10, the fluctuation of *LWC* above the γ layers in the sloped area (Figure 4c) started to mimic the one above the ground, but with a lower amplitude. This synchronism suggests that the sloped area's preferential pathway flow-through mode started weakening.
- M.E. 3. The sloped area showed a faster and more intense response to M.E. 3 starting March 17 than the flat area. Unlike the flat area, the slope's *LWC* fluctuation started exhibiting a strong diurnal pattern, whose peak occurred a couple of hours before the peak in air temperature and the peak in lysimeter outflow.
-

Overall, the TDR probes showed a faster and more intense response to air temperature warming episodes on the slope compared to the flat area, the presence of preferential pathways (particularly at the start of the ablation period), and a noticeably higher influence of solar radiation on the ablation of the sloped area compared to the flat one at the end of the study period.

~~TDR measurements of the snow's relative permittivity were normalized to the February 26 at 12:30 values to allow comparison between the different layers, areas and times (Figure 4). As described in the Methods Section, fast variations in relative permittivity are associated with a change in *LWC*. Timewise, we observe that the first mild episode, starting February 27, generated a tiny increase in *LWC* above the upper hard layer a day after it started. Interestingly, the lysimeter measured outflow at the base of the snowpack in the flat area 24 hours before any moisture increase was detected by the TDR probe placed on the ground in the flat area. Snowpack response to the February 28 ROS event occurred first at the bottom of the sloped area, followed by a limited increase in snow moisture above the hard snow layers. Detection of an increase in *LWC* at the base of the flat area occurred half a day after the increase for the sloped area, at a time that the air temperature had already dropped below zero. Past that time, normalized permittivity at all spots steadily decreased, reaching a plateau representative of the new dry densities of the snow layers. Differences observed in timing and amplitudes at the different probe locations suggest that liquid water flows followed preferential pathways, confirming what was assumed from *AWS* measurements. The *LWC* increased in response to the second mild episode, first at the base of the sloped area too. The increase was followed by an increase at the other probes 24 hours later, those above the β and γ layers being of very low amplitude. As was the case during the first mild episode, the strongest increase in *LWC* was measured over the sloped ground. At the end of the 10~~th~~ of March, three of the four probed layers showed an increase in *LWC*, which was more pronounced in the sloped area than in the flat area. After March 10, in the sloped area the fluctuation of *LWC* above the γ layers started to mimic the one aboveground, but with a lower amplitude. This synchronism suggests that the sloped area's preferential pathway flow-through mode started weakening. The sloped area showed a faster and more intense response to the mild episode starting March 17 compared to the flat area too. Unlike the flat area, the slope's *LWC* fluctuation started exhibiting a strong diurnal pattern, whose peak occurred a couple of hours before the peak in air temperature and the peak in lysimeter outflow. This suggests the slope was more responsive to the incoming solar radiation compared to the flat area.~~

~~Overall, the TDR probes showed a faster and more intense response to mild warming episodes on the slope compared to the flat area, the presence of preferential pathways (particularly at the start of the ablation period), and a noticeably higher influence of solar radiation on the ablations of the sloped area compared to the flat one at the end of the study period.~~

4.4~~3~~ Drone-based GPR permittivity measurement

For each survey day, each area, snow depth~~*h*~~ was extracted from the DSM following the north-to-south transects (Fig. 1b.) covered by the M600 pro during the GPR survey. Snow depth and snowpack bulk permittivity profiles of selected transects are shown in Figure 6~~5~~.

On February 26 (Figure 6a), the flat area shows quite stable bulk permittivity and snow depth profiles, with a relative permittivity ranging from 1.2 to 1.6. The slope transect exhibits slightly lower snow depth and higher bulk permittivity than the sloped section, between 1.4 and 2. The bulk permittivity over the sloped section appears more variable than the flat one too. With a relative permittivity ranging from 1.2 to 1.5 and from 1 to 2 for respectively the flat and the slope areas, ~~The~~ March 5 (Figure 6b) shows limited changes of bulk permittivity compared to ~~the 26th of~~ February 26 ~~for both variables and~~ for both areas.

The March 12 (Figure 6c) transects show a sharp change compared to the two first dates. Both areas exhibited a rise in bulk permittivity and a decrease in snow depth. Bulk permittivity profiles show gaps due to the GPR signal not penetrating fully through the wet snow. Ranging respectively from 1.9~~0.41~~ to 2.5~~0.78~~ and from 2 to 3.2 for the flat and the slope areas, the slope~~d~~ area bulk permittivity has higher values and variability ~~is more pronounced~~ than ~~of~~ the flat area. On March 19 (Figure 6d), the snow depth in the flat transects remained almost similar to that measured on March 12. The bulk permittivity decreased to values situated between those of March 5 and 12, reaching minimal relative permittivity values of 1.5 in both flat and slope areas, increasing the values ranges in both flat and slope areas. The slope~~d~~ area transect exhibited a decrease in bulk permittivity, like that of the flat area transect, and its variability remained higher than in the flat section. ~~On March 19, the~~The main difference between the two sections was the snow depth. The slope~~d~~ area showed a more pronounced decrease than the flat area. As no fresh precipitations were recorded between March 12 and 19, the decrease in permittivity in both sections can be interpreted as a decrease in *LWC*, which could have occurred together with snow densification in the sloped section.

Overall, Figure 6~~5~~ confirms the difference in response to ~~the mild event~~M.E. 2 ~~of March 11~~ between the snowpack's slope~~d~~ ~~area~~ and ~~the~~ flat area, including a high moisture content for both areas and a more pronounced densification of the snowpack over the slope~~d~~ area compared to the flat one~~area~~.

4.5~~3~~ Drone-based GPR frequency-dependent attenuation analysis

Contradicting snow temperature profiles (Figure 2c) that suggested the snowpack was dry, the *LWC* calculation and interpolation presented in Figure 7 suggested non-nulls *LWC* (ranging from 0 to 3.5%), with no visible differentiation between the sloped and flat areas on both February 26 (Figure 7a) and March 5 (Figure 7b). On both dates, there was a relative spatial heterogeneity in *LWC*, with no common patterns between the two dates.

On March 12 (Figure 7c), the flat area *LWC* ranged between 0 and 5.5%, while the slope area had *LWC* maximal values above 8%. The March 12 survey showed a general increase in *LWC* compared with the two previous surveys, and a differentiation between the two studied areas. The sloped area exhibited the highest overall LWC, although both areas were spatially variable. Compared to March 12, March 19 (Figure 7d) showed overall slightly lower *LWC* values in the sloped area compared to the flat area. However, the maximum value reached 6.5% in both areas, making them difficult to differentiate. *LWC* values remained highly variable for both sections, ranging between 0 and 6.5%.

Overall, Figure 7 confirms that, unlike the ROS event that occurred at the end of February, the sloped and flat areas responded in different ways to the March 11 ROS event. On the other hand, *LWC* values seem unrealistic for the two first survey dates that followed the pronounced cold episode. In a similar way, the absence of a recurrent spatial pattern in *LWC* variations between maps of different dates suggests the method was not able to capture these variations in a detailed way.

~~Results from the *LWC* calculation and interpolation are presented in Figure 6.~~

~~Contradicting snow temperature profiles and A2 measurements, Figure 6 suggests the February 26 and March 5 snowpacks present *LWC* ranging from 0 to 3% with no visible differentiation between the sloped and flat areas. Both dates show a relative spatial heterogeneity in *LWC* with no clear common patterns between the two dates.~~

~~The March 12 survey shows a general increase in *LWC* compared with the two previous surveys, and a differentiation between the two studied areas. The slope area exhibits the highest overall LWC, although both areas are spatially variable.~~

~~Compared to March 12, the *LWC* map for March 19 has lower values in the sloped area compared to the flat area, making both areas difficult to differentiate. *LWC* values remains highly variable for both sections.~~

~~Overall, Figure 6 confirms that, unlike the ROS event that occurred at the end of February, the sloped and flat areas responded in different ways to the March 11 ROS event. On the other hand, *LWC* non-null values seem unrealistic for the two first survey dates that followed the pronounced cold episode. In a similar way, the absence of a recurrent spatial pattern in *LWC* variations between maps of different dates suggests the method was not able to capture these variations in a detailed way.~~

5 Discussion

Drone-based estimation of key snowpack variables

The spatiotemporal variability in snow depth, snow density, *SWE* and snow *LWC*, four key properties of a snowpack, has been assessed using drone-based GPR and photogrammetry methods in a repeated way. Figure 8 provides an overview of the variability of those properties in the form of boxplots and, where possible, compares drone-based measurements to those of the AWS and from snow pits.

Photogrammetry snow depth results (Figure 8a) are in good agreement with those of the AWS and of the snow pits over the entire study period, with a possible slight overestimation in the two first surveys. The differences between the 25th and 75th percentiles in the flat area are systematically below 2 cm. For comparison, this difference is of the same order of magnitude as the one between the snow pit and AWS measurements and the median. The slope is characterized by a lower snow depth and a larger range than the flat area, especially after the ROS event that occurred on March 11. With most of the slope snow depth values below 40 cm the two last surveys, the estimated ±5 cm uncertainty that applies to the photogrammetry affects more than 12% of the measurement. Such high level of uncertainty may have potential detrimental effects on the GPR-based calculation of key snowpack properties.

The *LWC* boxplot in Figure 8b is effective in representing the general evolution of the snowpack moisture content through time: a stable situation occurring between the first two survey dates, followed by a marked increase in snow moisture on March 12 and a slight decrease on March 19 (for the sloped area only). The boxplot also successfully captures the difference in response to mild events between the flat and sloped areas. Compared to the A2 WISe sensor measurements, the boxplot shows the method did not succeed in providing realistic *LWC* values. According to the A2 measurements, snow pit bulk *LWC* values were close to 0% February 26, March 5 and March 12. while the GPR-based calculation medians for the flat area were 2, 1.5

and 4%, respectively. The differences between the 25th and 75th percentiles in the flat area were 1, 1.5 and 2% for the same dates. Even if the A2 measurements might have been influenced by the sampling constrains and therefore might have underestimated the snowpack average *LWC*, the drone-based result appears significantly overestimated.

Disagreement between GPR based calculations and reference measurements were observed for the relative snow density as well (Figure 8c). February 26 and March 5, the difference between reference values and GPR based calculation medians was 3 times higher than the difference between the 25th and 75th percentiles. The drone-based method underestimated relative snow density over the flat area compared with both the AWS and the snow pit measurements for the first two and the last dates, while overestimating it for March 12. Moreover, both the flat and sloped areas exhibited an unrealistic 50% decrease in snow relative density between March 12 and 18. No fresh snowfall occurred between those two dates.

Calculated as the product of h by ρ, *SWE* boxes show similar biases as relative snow density (Figure 8d).

Interestingly, we note that while Figure 6 shows the bulk permittivity profile being consistent with TDR and AWS measurements, this is not the case with the GPR-based computed variables presented in Figure 8. As described earlier, the bulk permittivity of the snowpack is influenced by both snow density and *LWC*. Figure 8 therefore suggests that the method we applied failed to differentiate the relative influence of both variables.

The method we applied makes use of empirical equations (7), (8) and (9), which are commonly used in snow hydrology. According to Tiuri et al. (1984), Equations (8) and (9) apply to pendular regime, for $\varepsilon_s' \leq 2.6$ ($\varepsilon_s' \leq 3$ for Colbeck (1982)), as opposed to a funicular regime. In a layered snowpack in which preferential flow occurs, it is realistic to hypothesize that both regimes occur in the snow column, making Equations (8) and (9) possibly not directly applicable to bulk relative permittivity measurements.

Different empirical formulas relating the relative permittivity to relative snow density have been subsequently developed (e.g. Di Paolo et al. (2018); Frolov and Macheret (1999)). They could possibly represent more accurate alternatives.

As suggested by Webb et al. (2021), reassessing the application conditions of the equation used in the present study is another direction that could be chosen. Selecting different equations depending on snowpack conditions and evolution over the winter could ensure a better use of these equations too.

Fixing the relative density of the snow based on manual sampling or AWS values could represent another solution to the problem encountered in differentiating between the relative influence of snow density and *LWC* on bulk permittivity. However, this solution would not allow for the capturing of the spatial variability in snow density, and therefore might bias calculations.

~~In the present study, the spatiotemporal variability in h, ρ, *SWE* and *LWC*, four key proprieties of a snowpack, has been assessed using drone-based GPR and photogrammetry methods in a repetitive way. Figure 7 provides an overview of the variability in a form of boxplots and, where possible, compares drone-based measurements to those of the AWS and from snow pits.~~

~~Photogrammetry results are in good agreement with those of the AWS and of the snow pits over the entire study period, with a possible slight overestimation in the two first surveys. Snow depth over the flat area consistently shows a narrow distribution. The slope is characterized by a lower snow depth and a larger variability than the flat, especially after the ROS event that occurred on March 11.~~

~~The *LWC* boxplots in Figure 7 represent well the general evolution of the snowpack moisture content through time: a stable situation occurring between the first two survey dates, followed by a marked increase in snow moisture on March 12 and a slight decrease on March 19 (for the sloped area only). The boxplot also captures the difference in response to mild events between the flat and sloped areas. Compared to the A2 measurements, the boxplots show the method is not able to provide realistic *LWC* absolute values. Even if we consider that the A2 measurements did not sample the entire snow column and therefore might have underestimated the snowpack average *LWC*, the drone-based result appears by far overestimated.~~

~~Although less obvious than for the *LWC*, ρ estimation appear to diverge from the reference measurements also. The drone-based method underestimates ρ over the flat area compared with both the AWS and the snow pit measurements for the first two and the last dates, while overestimating it for March 12. Moreover, both the flat and sloped areas exhibit an unrealistic 50% decrease in ρ between March 12 and 18, as no fresh snowfall occurred between those two dates.~~

~~Calculated as the product of *h* by ρ, *SWE* boxes show similar characteristics to ρ.~~

~~Interestingly, we note that while Figure 5 shows the bulk permittivity profile being coherent with TDR and AWS measurements, this was not the case anymore in the computed variables presented in Figure 7. As described earlier, the bulk permittivity of the snowpack is influenced by both ρ and *LWC*. Figure 7 therefore suggests that the method we applied failed to differentiate the relative influence of both variables.~~

~~Our method makes use of empirical Equations (6), (7) and (8), which are commonly used in snow hydrology. According to Tiuri et al. (1984), Equations (7) and (8) are valid in pendular regime, for $\varepsilon_s' \leq 2.6$ ($\varepsilon_s' \leq 3$ for Colbeck (1982)), as opposed to a funicular regime. In a layered snowpack in which preferential flow occurs, it is realistic to hypothesize that both regimes occur in the snow column, making Equations (7) and (8) possibly not directly applicable to bulk relative permittivity measurements. Different empirical formulas relating the relative permittivity to ρ have been subsequently developed (e.g. Di Paolo et al. (2018); Frolov and Macheret (1999)). In the present study, we decided to use the formulas presented in Tiuri et al. (1984) as they are most commonly used in the literature. Assessing the other formulas might be a way to improve the absolute values of key snowpack variables. As suggested by Webb et al. (2021), re-assessing the application conditions of the equation used in the present study is probably required.~~

~~Fixing the relative density of the snow based on manual sampling or AWS values could represent another solution to the problem met in differentiating between the relative influence of ρ and *LWC* on bulk permittivity. However, this solution would not allow for the capturing of the spatial variability in ρ and therefore might bias calculations.~~

Spatiotemporal variability in snowpack characteristics

TDR monitoring, drone-based photogrammetry and drone-based GPR have been shown to make a valuable combination for assessing the spatiotemporal variability in key snowpack variables. The use of photogrammetry to map snow depth over the study area has given the opportunity to calculate bulk permittivity from ~~repetitive~~repeated drone-based GPR surveys. Both bulk permittivity and snow depth profiles agreed with site observations and reference measurements. Converting the bulk permittivity into absolute snow density~~ρ~~, *LWC* and *SWE* values do not provide the expected results even if the temporal evolution of those parameters was captured in an acceptable way. TDR monitoring complemented the drone-based measurements, providing both high temporal resolution and layer-based snowpack relative permittivity time series. ~~Except for the ρ, *LWC* and *SWE* calculations,~~ Snow depth and snow bulk permittivity calculations were highly consistent from ~~the~~comparing the different methods ~~were highly consistent compared~~ to each other, allowing for the capture of the flat and slope~~d~~ areas responses to changes in meteorological conditions.

Points learned from the case study

The application of the proposed methodology to the winter 2020-21 led to the following facts being learned:

- The flat and sloped areas had comparable responses to the first ROS event of the study period, which occurred on a cold and dry snowpack at the end of February. That event produced snowpack outflows and increases in *LWC*, especially at the base of both areas. The slope area, however, showed a faster and more intense response than the flat one.
- The first ROS episode did not modify the snowpack's snow density and snow depth profiles in a substantial way. Both study areas exhibited characteristics of preferential flow pathways.
- The second ROS event that occurred on March 10 on an already pre-warmed snowpack affected the sloped area in a different way than the flat one, both areas showing important differences in snow depth, *LWC* and density in the March 12 surveys. The timing and amplitude of the outflow suggest a more homogeneous flow path was present than during the first ROS.
- The third mild episode that occurred from March 16 to 18 did not drastically modify the characteristics of either area compared to the March 12 situation. However, the slope showed faster rates of melt/ablation and showed higher response to diurnal fluctuations, probably due to its southerly aspect.

~~More precisely, the results obtained in this study show that:~~

- ~~The flat and sloped areas had comparable responses to the first ROS event of the study period, which occurred at the end of February. That event produced snowpack outflows and increases in *LWC*, especially at the base of both areas. The sloped area, however, showed a faster and more intense response than the flat one.~~
- ~~The first ROS episode did not modify the snowpack's ρ and h profiles in a substantial way. Both study areas exhibited characteristics of preferential flow pathways.~~
- ~~The second ROS event that occurred on March 10 affected the sloped area in a different way than the flat one, both areas showing important differences in h, *LWC* and ρ in the March 12 surveys.~~
- ~~The third mild episode that occurred from March 16 to 18 did not drastically modify the characteristics of both areas compared to the March 12 situation. However, the slope showed faster rates of melt/ablation, probably due to its southward orientation.~~

6 Conclusion

A combination of TDR monitoring, drone-based photogrammetry and drone-based GPR was used in the experimental watershed of Ste-Marthe (Quebec, Canada) over the winter of 2020–2021. The suite of methods showed comparable snow accumulation over flat and sloped areas, with comparable characteristics lasting after the first ROS event. The second ROS event at the start of the ablation season led to differences in response between the two areas.

Drone-based GPR showed being~~was~~ very instructive when interpretation was based on bulk permittivity results but showed limitations for mapping snow density~~*ρ*~~, *SWE* and *LWC*. There are questions about the applicability of empirical equations used given the site conditions. The results suggest the empirical equations should be reassessed for conditions that differ from the ones they were formulated for. The method did not allow getting the full benefit from applying the GPR frequency dependant attenuation method to estimate *LWC* in snowpack. The method however shows promise. In the 2020-2021 winter, the radargram obtained using a 1.5 GHz GPR was not detailed enough to differentiate between the main snowpack layers. However, efforts should be continued in this regard, as the 2020–2021 snowpack was characterized by a relatively low snow depth and an uneven distr~~pos~~ibution of the ice layers in the snow column.

Author contributions

MB, ER and FB framed the research project, fixed the objectives and made the research project steering group. EV designed the research and organized the fieldwork. EV and MB collected data in the field. CM conducted a substantial part of the GPR data treatment. EV produced all the other results and made the interpretation. EV w~~W~~rote the initial draft of the paper. All authors contributed to editing and revising the paper.

Code/Data availability

The data are available on request to the corresponding author.

Competing interests

The authors declare that they have no conflict of interest.

Acknowledgment

This research is supported by the Geochemistry and Geodynamics Research Centre (Geotop) of Quebec; the Quebec Water Research Center (Centreau); FRQNT and the Natural Sciences and Engineering Research Council of Canada (NSERC); and the Ecole de Technologie Superieure, a member of the Université du Quebec. The authors are grateful for the invaluable support of the municipality of Sainte-Marthe, Quebec, Canada.

References

Andradóttir, H. Ó., Arnardóttir, A. R., and Zaqout, T.: Rain on snow induced urban floods in cold maritime climate: Risk, indicators and trends, Hydrological Processes, 35, e14298, https://doi.org/10.1002/hyp.14298, 2021.

Avanzi, F., Bianchi, A., Cina, A., De Michele, C., Maschio, P., Pagliari, D., Passoni, D., Pinto, L., Piras, M., and Rossi, L.: Centimetric Accuracy in Snow Depth Using Unmanned Aerial System Photogrammetry and a MultiStation, Remote Sensing, 10, 765, 2018.

Bradford, J. H.: Frequency-Dependent Attenuation Analysis of Ground-Penetrating Radar Data, John H. Bradford, 72, 10.1190/1.2710183, 2007.

Bradford, J. H., Harper, J. T., and Brown, J.: Complex dielectric permittivity measurements from ground-penetrating radar data to estimate snow liquid water content in the pendular regime, Water Resources Research, 45, 10.1029/2008wr007341, 2009.

Brown, R., Tapsoba, D., and Derksen, C.: Evaluation of snow water equivalent datasets over the Saint-Maurice river basin region of southern Québec, Hydrological Processes, 32, 2748-2764, 10.1002/hyp.13221, 2018.

Bühler, Y., Adams, M., Bösch, R., and Stoffel, A.: Mapping snow depth in alpine terrain with unmanned aerial systems (UAS): potential and limitations, The Cryosphere Discussions, 10.5194/tc-2015-220, 2016a.

Bühler, Y., Stoffel, A., Adams, M., Bösch, R., and Ginzler, C.: UAS Photogrammetry of Homogenous Snow Cover, 2016b.

Chen, P., Li, Z., and Zheng, N.: A New Approach for GNSS-IR Snow Depth Monitoring With Slope Correction and Error Prediction, 10.21203/rs.3.rs-150402/v1, 2021.

Cho, E., McCrary, R. R., and Jacobs, J. M.: Future Changes in Snowpack, Snowmelt, and Runoff Potential Extremes Over North America, Geophysical Research Letters, 48, 10.1029/2021gl094985, 2021.

Colbeck, S. C.: The geometry and permittivity of snow at high frequencies, Journal of Applied Physics, 53, 4495-4500, 10.1063/1.331186, 1982.

Conger, S. M. and McClung, D. M.: Comparison of density cutters for snow profile observations, Journal of Glaciology, 55, 163-169, 10.3189/002214309788609038, 2009.

Deems, J. S., Painter, T. H., and Finnegan, D. C.: Lidar measurement of snow depth: a review, Journal of Glaciology, 59, 467-479, 10.3189/2013JoG12J154, 2017.

Denoth, A.: An electron device for long-term snow wetness recording, International Journal of Rock Mechanics and Mining Sciences and Geomechanics Abstracts, 32, 144A-145A, 10.1016/0148-9062(95)90311-R, 1995.

DeWalle, D. R. and Rango, A.: Principles of Snow Hydrology, Cambridge University Press2008.

Di Paolo, F., Cosciotti, B., Lauro, S., Mattei, E., and Pettinelli, E.: Dry snow permittivity evaluation from density: A critical review, 1-5 pp., 10.1109/ICGPR.2018.8441610, 2018.

Dierauer, J. R., Allen, D. M., and Whitfield, P. H.: Climate change impacts on snow and streamflow drought regimes in four ecoregions of British Columbia, Canadian Water Resources Journal / Revue canadienne des ressources hydriques, 46, 168-193, 10.1080/07011784.2021.1960894, 2021.

Dietz, A. J., Kuenzer, C., Gessner, U., and Dech, S.: Remote sensing of snow – a review of available methods, International Journal of Remote Sensing, 33, 4094-4134, 10.1080/01431161.2011.640964, 2012.

Ding, Y., Mu, C., Wu, T., Hu, G., Zou, D., Wang, D., Li, W., and Wu, X.: Increasing cryospheric hazards in a warming climate, Earth-Science Reviews, 213, 103500, https://doi.org/10.1016/j.earscirev.2020.103500, 2021.

Dingman, S.: Hydrologic Effects of Frozen Ground: Literature Review and Synthesis, 60, 1975.

Doesken, N. J., Ryan, W. A., and Fassnacht, S. R.: Evaluation of Ultrasonic Snow Depth Sensors for U.S. Snow Measurements, Journal of Atmospheric and Oceanic Technology, 25, 667-684, 10.1175/2007jtecha947.1, 2008.

Evans, S. L., Flores, A. N., Heilig, A., Kohn, M. J., Marshall, H. P., and McNamara, J. P.: Isotopic evidence for lateral flow and diffusive transport, but not sublimation, in a sloped seasonal snowpack, Idaho, USA, Geophysical Research Letters, 43, 3298-3306, 10.1002/2015gl067605, 2016.

Fierz, C., R.L, A., Y, D., P, E., Greene, E., McClung, D., Nishimura, K., Satyawali, P., and Sokratov, S.: The international classification for seasonal snow on the ground (UNESCO, IHP (International Hydrological Programme)–VII, Technical Documents in Hydrology, No 83; IACS (International Association of Cryospheric Sciences) contribution No 1), 2009.

Ford, C. M., Kendall, A. D., and Hyndman, D. W.: Snowpacks decrease and streamflows shift across the eastern US as winters warm, Science of The Total Environment, 793, 148483, https://doi.org/10.1016/j.scitotenv.2021.148483, 2021.

Foster, J., Sun, C., Walker, J., Kelly, R., Chang, A., Dong, J., and Powell, H.: Quantifying the uncertainty in passive microwave snow water equivalent observations, Remote Sensing of Environment, 94, 187-203, 10.1016/j.rse.2004.09.012, 2005.

Frolov, A. D. and Macheret, Y.: On dielectric properties of dry and wet snow, Hydrological Processes, 13, 1755-1760, 10.1002/(SICI)1099-1085(199909)13:12/13<1755::AID-HYP854>3.0.CO;2-T, 1999.

Gergel, D. R., Nijssen, B., Abatzoglou, J. T., Lettenmaier, D. P., and Stumbaugh, M. R.: Effects of climate change on snowpack and fire potential in the western USA, Climatic Change, 141, 287-299, 10.1007/s10584-017-1899-y, 2017.

Gergely, M., Schneebeli, M., and Roth, K.: First experiments to determine snow density from diffuse near-infrared transmittance, Cold Regions Science and Technology, 64, 81-86, 10.1016/j.coldregions.2010.06.005, 2010.

Godio, A., Frigo, B., Chiaia, B., Maggioni, P., Freppaz, M., Ceaglio, E., and Dellavedova, P.: Integration of upward GPR and water content reflectometry to monitor snow properties, Near Surface Geophysics, 16, 154-163, 10.3997/1873-0604.2017060, 2018.

Goodison, B. E., Glynn, J. E., Harvey, K. D., and Slater, J. E.: Snow Surveying in Canada: A Perspective, Canadian Water Resources Journal, 12, 27-42, 10.4296/cwrj1202027, 1987.

Guneriussen, T., Høgda, K., and Lauknes, I.: InSAR for estimation of changes in snow water equivalent of dry snow, Geoscience and Remote Sensing, IEEE Transactions on, 39, 2101-2108, 10.1109/36.957273, 2001.

Hao, J., Mind'je, R., Feng, T., and Li, L.: Performance of snow density measurement systems in snow stratigraphies, Hydrology Research, 52, 834-846, 10.2166/nh.2021.133, 2021.

Harder, P., Pomeroy, J., and Helgason, W.: Improving sub-canopy snow depth mapping with unmanned aerial vehicles: lidar versus structure-from-motion techniques, The Cryosphere, 14, 1919-1935, 10.5194/tc-14-1919-2020, 2020.

Hawley, R., Brandt, O., Morris, E., Kohler, J., Shepherd, A., and Wingham, D.: Instruments and Methods Techniques for measuring high-resolution firn density profiles: case study from Kongsvegen, Svalbard, Journal of Glaciology, 54, 463-468, 10.3189/002214308785837020, 2008.

Hodgkins, G. A. and Dudley, R. W.: Changes in late-winter snowpack depth, water equivalent, and density in Maine, 1926–2004, Hydrological Processes, 20, 741-751, https://doi.org/10.1002/hyp.6111, 2006.

Holbrook, W. S., Miller, S. N., and Provart, M. A.: Estimating snow water equivalent over long mountain transects using snowmobile-mounted ground-penetrating radar, Geophysics, 81, WA183-WA193, 10.1190/geo2015-0121.1, 2016.

Jacobs, J. M., Hunsaker, A. G., Sullivan, F. B., Palace, M., Burakowski, E. A., Herrick, C., and Cho, E.: Snow depth mapping with unpiloted aerial system lidar observations: a case study in Durham, New Hampshire, United States, The Cryosphere, 15, 1485-1500, 10.5194/tc-15-1485-2021, 2021.

Jenssen, R. O. R. and Jacobsen, S.: Drone-mounted UWB snow radar: technical improvements and field results, Journal of Electromagnetic Waves and Applications, 34, 1930-1954, 10.1080/09205071.2020.1799871, 2020.

Kinar, N. and Pomeroy, J.: SAS2: the system for acoustic sensing of snow: SAS2: The System for Acoustic Sensing of Snow, Hydrological Processes, 29, 10.1002/hyp.10535, 2015a.

Kinar, N. and Pomeroy, J.: Measurement of the physical properties of the snowpack, Reviews of Geophysics, 53, 481-544, 10.1002/2015rg000481, 2015b.

Koutantou, K., Mazzotti, G., and Brunner, P.: Uav-Based Lidar High-Resolution Snow Depth Mapping in the Swiss Alps: Comparing Flat and Steep Forests, The International Archives of the Photogrammetry, Remote Sensing and Spatial Information Sciences, XLIII-B3-2021, 477-484, 10.5194/isprs-archives-XLIII-B3-2021-477-2021, 2021.

Leppänen, L., Kontu, A., Hannula, H.-R., Sjöblom, H., and Pulliainen, J.: Sodankylä manual snow survey program, Geoscientific Instrumentation, Methods and Data Systems, 5, 163-179, 10.5194/gi-5-163-2016, 2016.

Li, D., Lettenmaier, D. P., Margulis, S. A., and Andreadis, K.: The Role of Rain-on-Snow in Flooding Over the Conterminous United States, Water Resources Research, 55, 8492-8513, 10.1029/2019wr024950, 2019.

Lindström, G., Pers, C., Rosberg, J., Strömqvist, J., and Arheimer, B.: Development and testing of the HYPE (Hydrological Predictions for the Environment) water quality model for different spatial scales, Hydrology Research, 41, 295-319, 10.2166/nh.2010.007, 2010.

Liu, J. and Lobb, D. A.: An Overview of Crop and Crop Residue Management Impacts on Crop Water Use and Runoff in the Canadian Prairies, Water, 13, 10.3390/w13202929, 2021.

Lundberg, A., Kruglyak, A., Gustafsson, D., and Sundström, N.: Field evaluation of a new method for estimation of liquid water content and snow water equivalent of wet snowpacks with GPR, Hydrology Research, 44, 600-613, 10.2166/nh.2012.182, 2013.

Lundberg, A., Gustafsson, D., Stumpp, C., Klöve, B., and Feiccabrino, J.: Spatiotemporal Variations in Snow and Soil Frost—A Review of Measurement Techniques, Hydrology, 3, 28, 10.3390/hydrology3030028, 2016.

Magnusson, J., Jonas, T., López-Moreno, I., and Lehning, M.: Snow cover response to climate change in a high alpine and half-glacierized basin in Switzerland, Hydrology Research, 41, 230-240, 10.2166/nh.2010.115, 2010.

Mas, A., Baraer, M., Arsenault, R., Poulin, A., and Préfontaine, J.: Targeting high robustness in snowpack modeling for Nordic hydrological applications in limited data conditions, Journal of Hydrology, 564, 1008-1021, https://doi.org/10.1016/j.jhydrol.2018.07.071, 2018.

Mavrovic, A., Madore, J.-B., Langlois, A., Royer, A., and Roy, A.: Snow liquid water content measurement using an open-ended coaxial probe (OECP), Cold Regions Science and Technology, 171, 10.1016/j.coldregions.2019.102958, 2020.

Morris, E. and Cooper, J.: Instruments and Methods Density measurements in ice boreholes using neutron scattering, Journal of Glaciology, 49, 599-604, 10.3189/172756503781830403, 2003.

Morse, B. and Turcotte, B.: Risque d'inondations par embâcles de glaces et estimations des débits hivernaux dans un contexte de changements climatiques, Rapport présenté à Ouranos, 2018.

Mortimer, C., Mudryk, L., Derksen, C., Luojus, K., Brown, R., Kelly, R., and Tedesco, M.: Evaluation of long-term Northern Hemisphere snow water equivalent products, The Cryosphere, 14, 1579-1594, 10.5194/tc-14-1579-2020, 2020.

Najafi, M. R., Zwiers, F., and Gillett, N.: Attribution of the Observed Spring Snowpack Decline in British Columbia to Anthropogenic Climate Change, Journal of Climate, 30, 4113-4130, 10.1175/jcli-d-16-0189.1, 2017.

Neal, A.: Ground-penetrating radar and its use in sedimentology: Principles, problems and progress, Earth-Science Reviews, 66, 261-330, 10.1016/j.earscirev.2004.01.004, 2004.

Paquotte, A. and Baraer, M.: Hydrological behaviour of an ice-layered snowpack in a non-mountainous environment, Hydrological Processes, 36, 10.1002/hyp.14433, 2022.

Pérez Díaz, C. L., Muñoz, J., Lakhankar, T., Khanbilvardi, R., and Romanov, P.: Proof of Concept: Development of Snow Liquid Water Content Profiler Using CS650 Reflectometers at Caribou, ME, USA, Sensors, 17, 647, 2017.

Prager, S., Sexstone, G., McGrath, D., Fulton, J., and Moghaddam, M.: Snow Depth Retrieval With an Autonomous UAV-Mounted Software-Defined Radar, IEEE Transactions on Geoscience and Remote Sensing, 60, 1-16, 10.1109/tgrs.2021.3117509, 2022.

Previati, M., Godio, A., and Ferraris, S.: Validation of spatial variability of snowpack thickness and density obtained with GPR and TDR methods, Journal of Applied Geophysics, 75, 284-293, 10.1016/j.jappgeo.2011.07.007, 2011.

Prokop, A.: Assessing the applicability of terrestrial laser scanning for spatial snow depth measurements, Cold Regions Science and Technology, 54, 155-163, 10.1016/j.coldregions.2008.07.002, 2008.

Quéno, L., Fierz, C., van Herwijnen, A., Longridge, D., and Wever, N.: Deep ice layer formation in an alpine snowpack: monitoring and modeling, The Cryosphere, 14, 3449-3464, 10.5194/tc-14-3449-2020, 2020.

Revuelto, J., López-Moreno, J. I., Azorin-Molina, C., and Vicente-Serrano, S. M.: Canopy influence on snow depth distribution in a pine stand determined from terrestrial laser data, Water Resources Research, 51, 3476-3489, 10.1002/2014wr016496, 2015.

Rott, H., Nagler, T., and Scheiber, R.: Snow mass retrieval by means of SAR interferometry, 2003.

Royer, A., Roy, A., Jutras, S., and Langlois, A.: Review article: Performance assessment of radiation-based field sensors for monitoring the water equivalent of snow cover (SWE), The Cryosphere, 15, 5079-5098, 10.5194/tc-15-5079-2021, 2021.

Sihvola, A. and Tiuri, M.: Snow Fork for Field Determination of the Density and Wetness Profiles of a Snow Pack, Geoscience and Remote Sensing, IEEE Transactions on, 24, 717-721, 10.1109/TGRS.1986.289619, 1986.

Stacheder, M., Koeniger, F., and Schuhmann, R.: New Dielectric Sensors and Sensing Techniques for Soil and Snow Moisture Measurements, Sensors, 9, 2951-2967, 2009.

Sturm, M. and Holmgren, J.: An Automatic Snow Depth Probe for Field Validation Campaigns, Water Resources Research, 54, 9695-9701, https://doi.org/10.1029/2018WR023559, 2018.

Sun, F., Berg, N., Hall, A., Schwartz, M., and Walton, D.: Understanding End-of-Century Snowpack Changes Over California's Sierra Nevada, Geophysical Research Letters, 46, 933-943, https://doi.org/10.1029/2018GL080362, 2019.

Tiuri, M., Sihvola, A., Nyfors, E., and Hallikaiken, M.: The complex dielectric constant of snow at microwave frequencies, IEEE Journal of Oceanic Engineering, 9, 377-382, 10.1109/joe.1984.1145645, 1984.

Turner, G. and Siggins, A. F.: Constant Q attenuation of subsurface radar pulses, GEOPHYSICS, 59, 1192-1200, 10.1190/1.1443677, 1994.

Valence and Baraer: Impact of the Spatial and Temporal Variability of Snowpack Condition on Internal Liquid Water Fluxes, 2021.

Vionnet, V., Mortimer, C., Brady, M., Arnal, L., and Brown, R.: Canadian historical Snow Water Equivalent dataset (CanSWE, 1928–2020), Earth System Science Data, 13, 4603-4619, 10.5194/essd-13-4603-2021, 2021.

Webb, R. W., Wigmore, O., Jennings, K., Fend, M., and Molotch, N. P.: Hydrologic connectivity at the hillslope scale through intra-snowpack flow paths during snowmelt, Hydrological Processes, 34, 1616-1629, 10.1002/hyp.13686, 2020.

Webb, R. W., Marziliano, A., McGrath, D., Bonnell, R., Meehan, T. G., Vuyovich, C., and Marshall, H.-P.: In Situ Determination of Dry and Wet Snow Permittivity: Improving Equations for Low Frequency Radar Applications, Remote Sensing, 13, 10.3390/rs13224617, 2021.

Yildiz, S., Akyurek, Z., and Binley, A.: Quantifying snow water equivalent using terrestrial ground penetrating radar and unmanned aerial vehicle photogrammetry, Hydrological Processes, 35, 10.1002/hyp.14190, 2021.

Yu, K., Li, Y., Jin, T., Chang, X., Wang, Q., and Li, J.: GNSS-R-Based Snow Water Equivalent Estimation with Empirical Modeling and Enhanced SNR-Based Snow Depth Estimation, Remote Sensing, 12, 10.3390/rs12233905, 2020.

Zhang, G., Yao, T., Xie, H., Wang, W., and Yang, W.: An inventory of glacial lakes in the Third Pole region and their changes in response to global warming, Global and Planetary Change, 131, 148-157, https://doi.org/10.1016/j.gloplacha.2015.05.013, 2015.

965

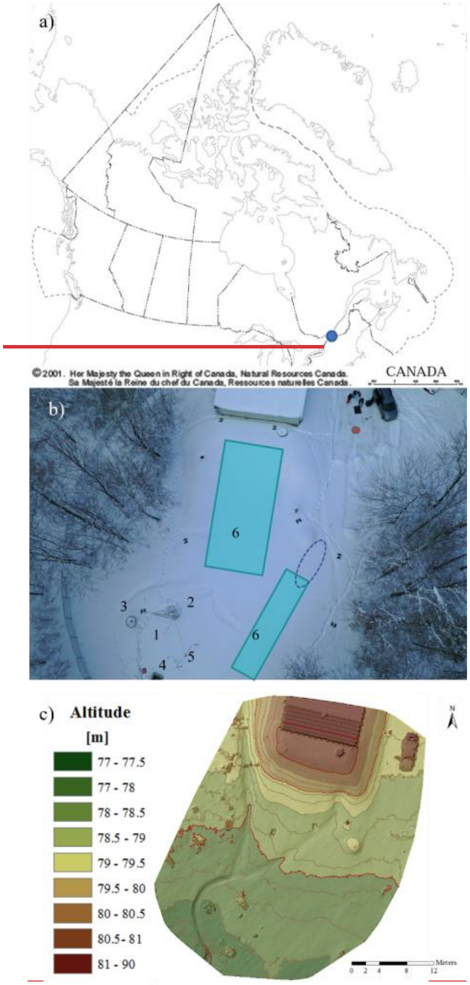

a mis en forme : Titre 1, Pas de paragraphes solidaires

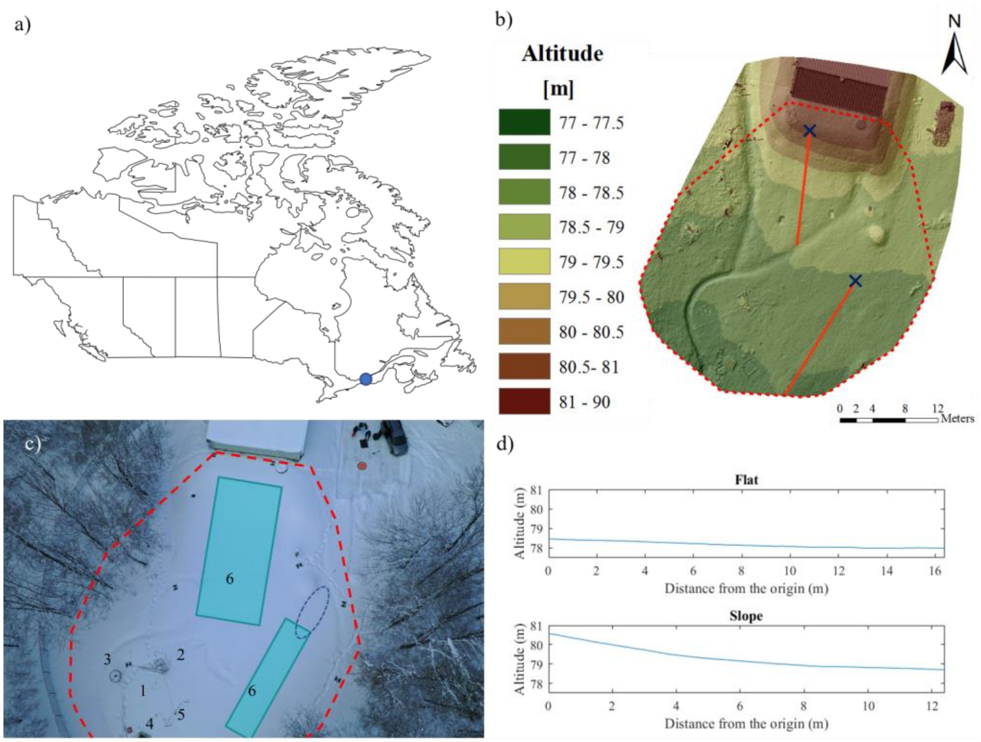

Figure 1: Study Site. a) Location of the BVE Ste-Marthe. b) Snow-free DSM of the main station area; red polygon delimits the study area, red lines represent the two studied transects and blue cross mark the two profiles origins. c~~b~~) Overview of the BVE Ste-Marthe main station; red polygon delimits the study area, blue areas represent the two studied areas and dashed dark blue ellipse represent the zone used for snow pit. Numbers identify devices of interest for the present study: (1) sonic sensor, (2) ground and snow temperature sensors, (3) shielded precipitation gauge, (4) snow lysimeter, (5) *SWE* sensor and (6) TDRs. ~~c) DSM of the main station area.~~d) Altitude profile of the two studied transects

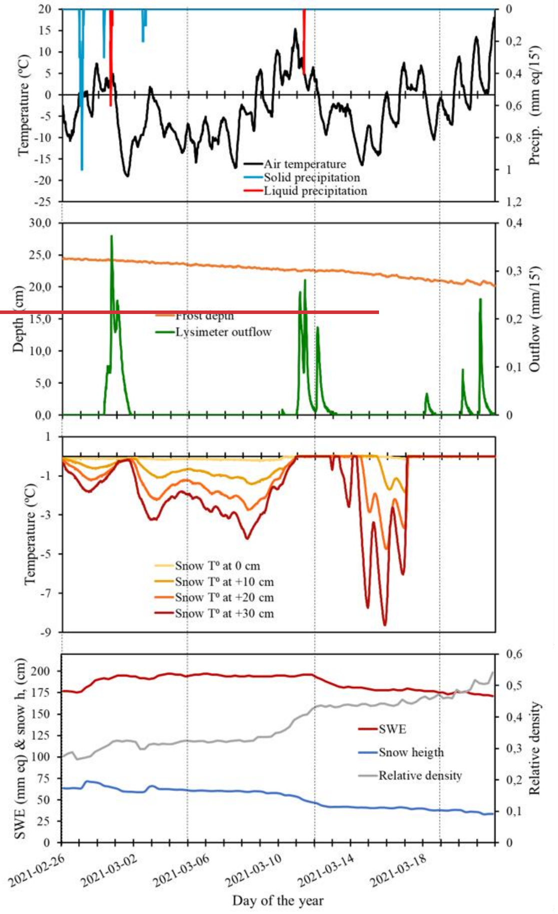
Temperature (ºC)
Precip. (mm eq/15')
Air temperature
Solid precipitation
Liquid precipitation
20
15
10
5
0
-5
-10
-15
-20
-25
0
0,2
0,4
0,6
0,8
1
1,2
Depth (cm)
Outflow (mm/15')
Frost depth
Lysimeter outflow
30,0
25,0
20,0
15,0
10,0
5,0
0,0
0,4
0,3
0,2
0,1
0
Temperature (ºC)
Snow Tº at 0 cm
Snow Tº at +10 cm
Snow Tº at +20 cm
Snow Tº at +30 cm
1
-1
-3
-5
-7
-9
SWE (mm eq) & snow h, (cm)
Relative density
SWE
Snow heigth
Relative density
200
175
150
125
100
75
50
25
0
0,6
0,5
0,4
0,3
0,2
0,1
0
2021-02-26
2021-03-02
2021-03-06
2021-03-10
2021-03-14
2021-03-18
Day of the year

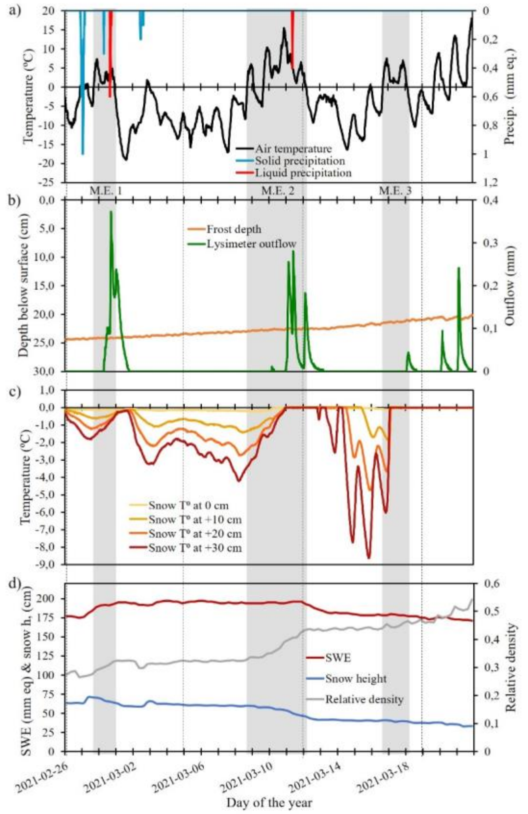

Figure 2~~2~~: AWS measurements during the winter 2022 ablation period. a) Air temperature and precipitations; b) frost depth and lysimeter outflow; c) snow temperature at 4 different height; d) Snow water equivalent, snow height and snow relative density. Variables' associated to the different line colours are indicated in each subfigure. Semi-transparent grey shadings represent mild episodes. Mild episodes identification is given underneath sub-figure a). Details about variables' descriptions and measurements are given in Table 1.~~AWS measurements during the winter 2022 ablation period.~~ Vertical dashed lines indicate field measurements days.~~ Variables' names are indicated in each subfigure. Details about variables' descriptions and measurements are given in Table 1.~~

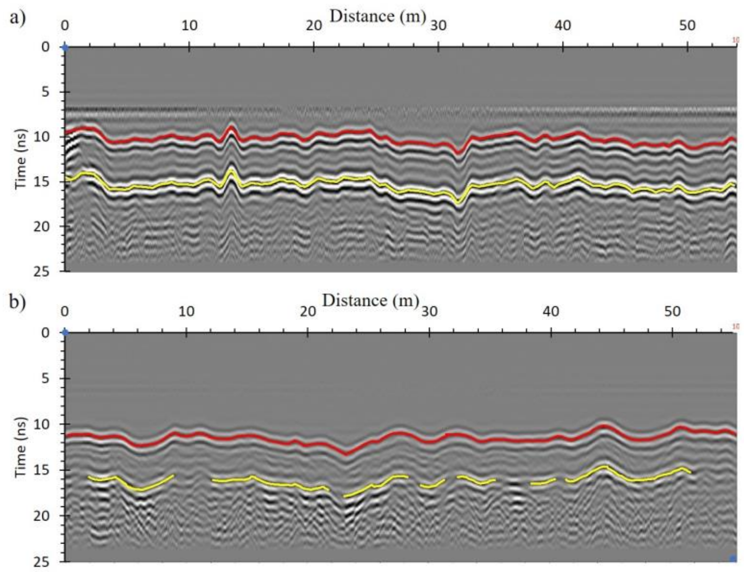

Figure 3: Flat area drone-based 1,5GHz GPR radargram collected on a) the 5th of March. b) the 12th of March (considered as the less legible radargram). The red line represents the air-snow interface and the yellow line represents the snow-ground interface.

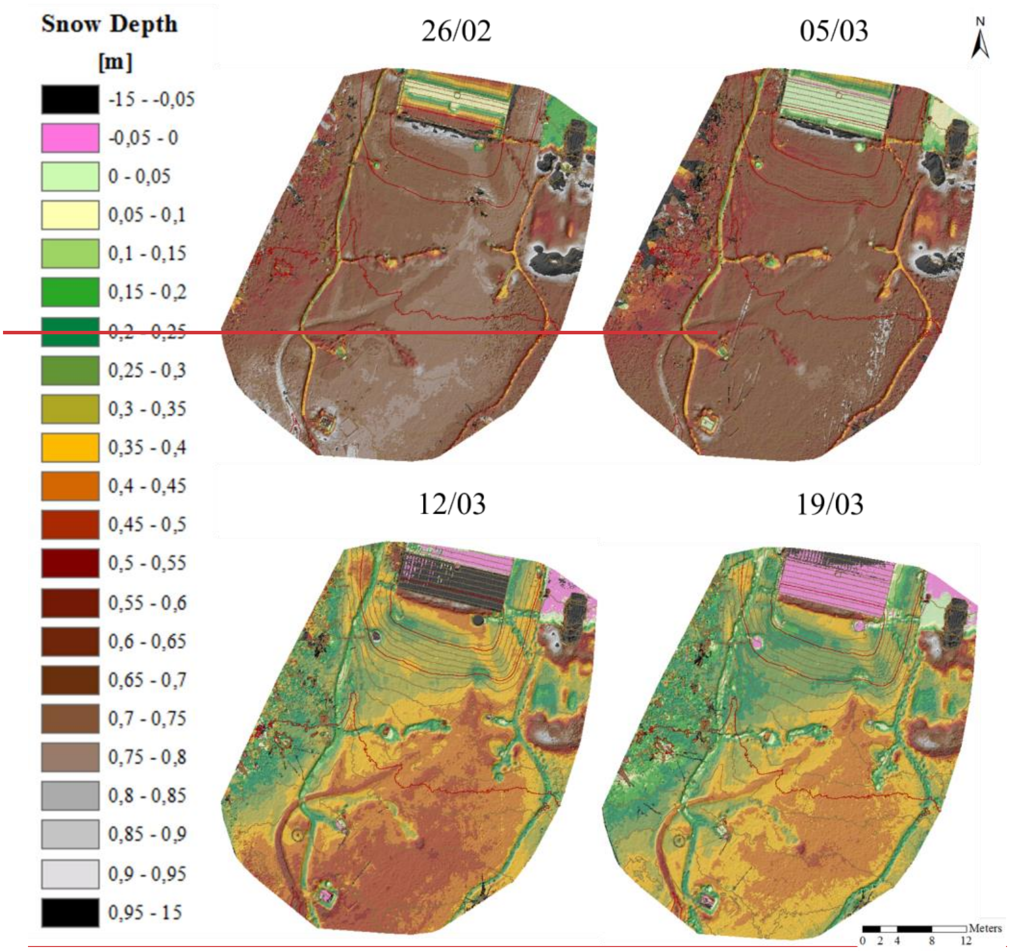
Snow Depth
[m]
-15 - -0,05
-0,05 - 0
0 - 0,05
0,05 - 0,1
0,1 - 0,15
0,15 - 0,2
0,2 - 0,25
0,25 - 0,3
0,3 - 0,35
0,35 - 0,4
0,4 - 0,45
0,45 - 0,5
0,5 - 0,55
0,55 - 0,6
0,6 - 0,65
0,65 - 0,7
0,7 - 0,75
0,75 - 0,8
0,8 - 0,85
0,85 - 0,9
0,9 - 0,95
0,95 - 15
26/02
05/03
N
12/03
19/03
Meters
0 2 4 8 12

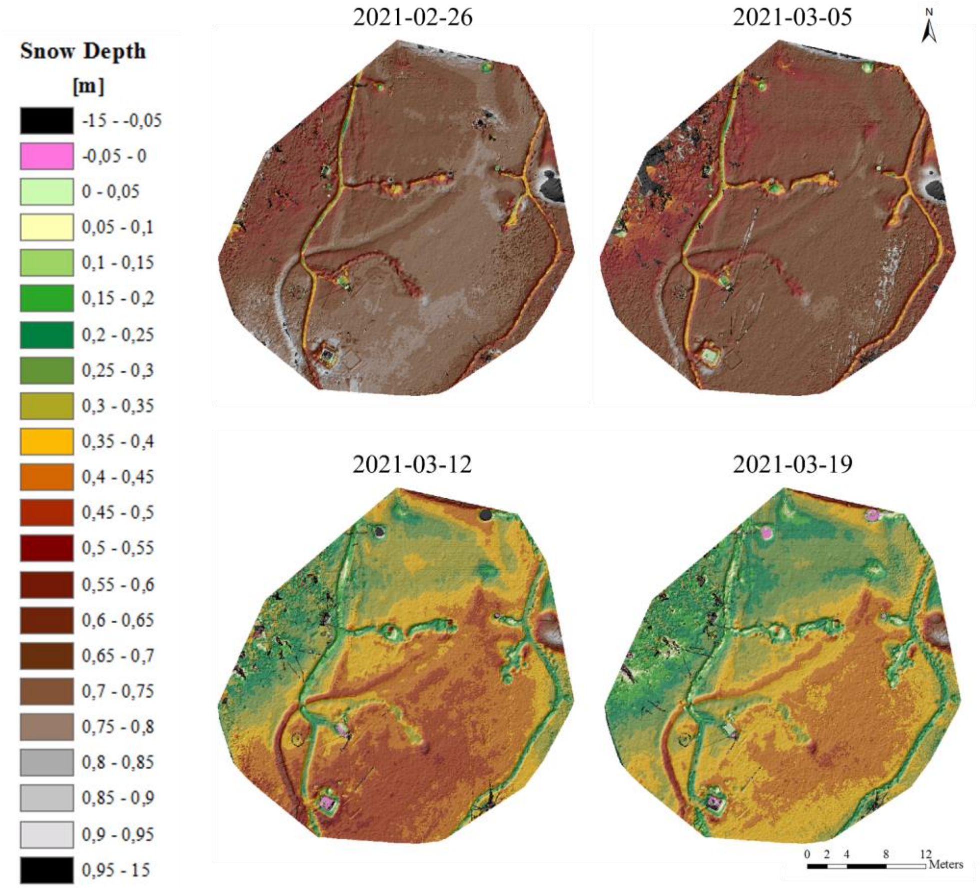

Figure 4~~3~~: Snow depth calculated by photogrammetry for the four dates covered in this study.

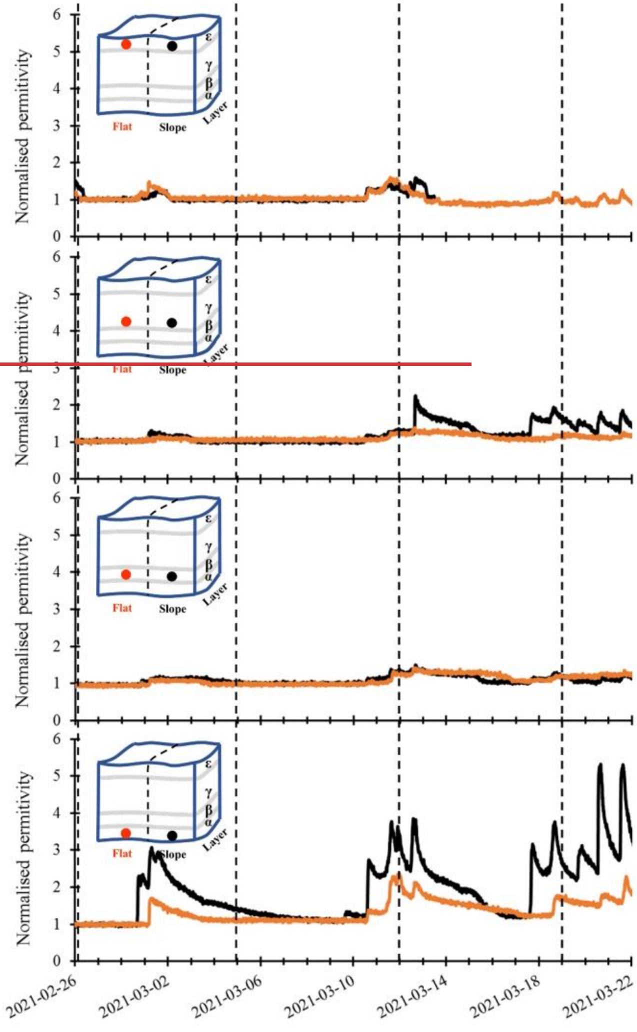
Normalised permitivity
0
1
2
3
4
5
6
ε
γ
β
α
Layer
Flat
Slope
2021-02-26
2021-03-02
2021-03-06
2021-03-10
2021-03-14
2021-03-18
2021-03-22

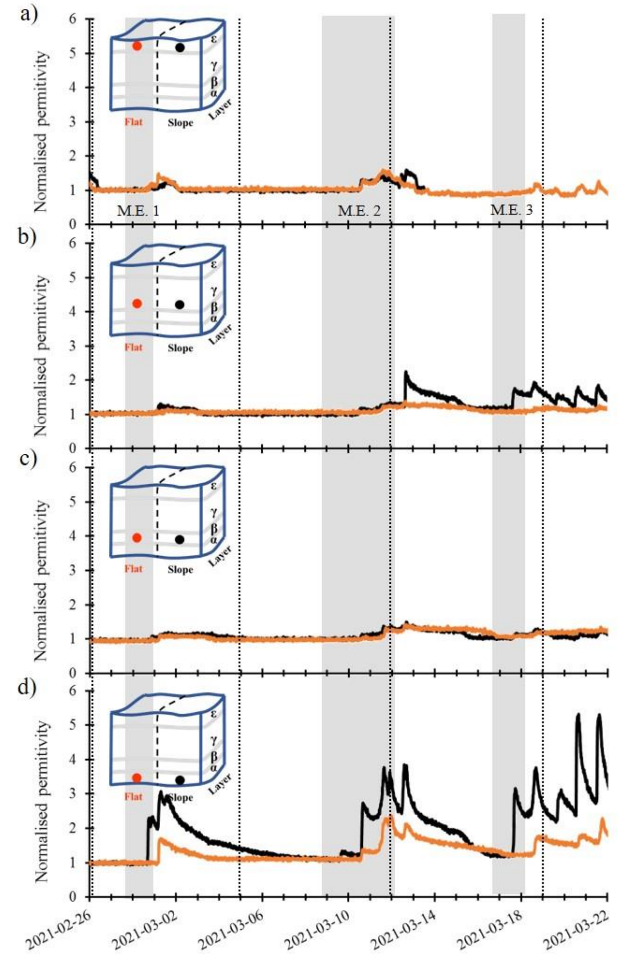

Figure 5~~4~~: Normalized permittivity measured by TDR probes in the sloped (black line) and flat sections (orange line). Probe positions in each graph are shown in drawings representing a simplified description of the snowpack with layers identification letters. a) layer ε; b) layer γ; c) layer β and d) layer α. Semi-transparent grey shadings represent mild episodes. Mild episodes identification is given at sub-figure a). Vertical dashed lines mark field visit dates.~~Normalized permittivity measured by TDR probes in the sloped and flat sections. Probe positions in each graph are shown in drawings representing a simplified description of the snowpack. Vertical dashed lines mark field visit dates.~~

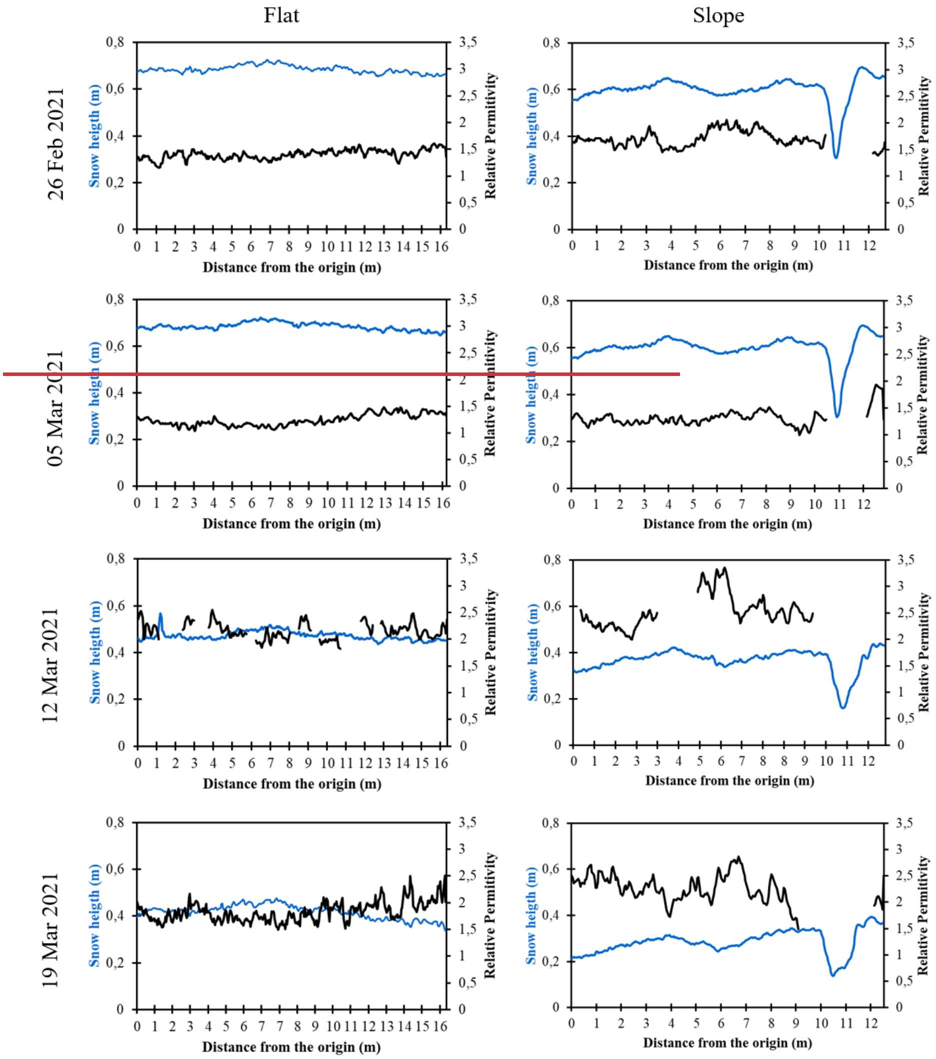

Flat
Slope
26 Feb 2021
05 Mar 2021
12 Mar 2021
19 Mar 2021
Snow heigth (m)
Relative Permittivity
Distance from the origin (m)
0
0,2
0,4
0,6
0,8
0,5
1
1,5
2
2,5
3
3,5
0 1 2 3 4 5 6 7 8 9 10 11 12 13 14 15 16
0 1 2 3 4 5 6 7 8 9 10 11 12

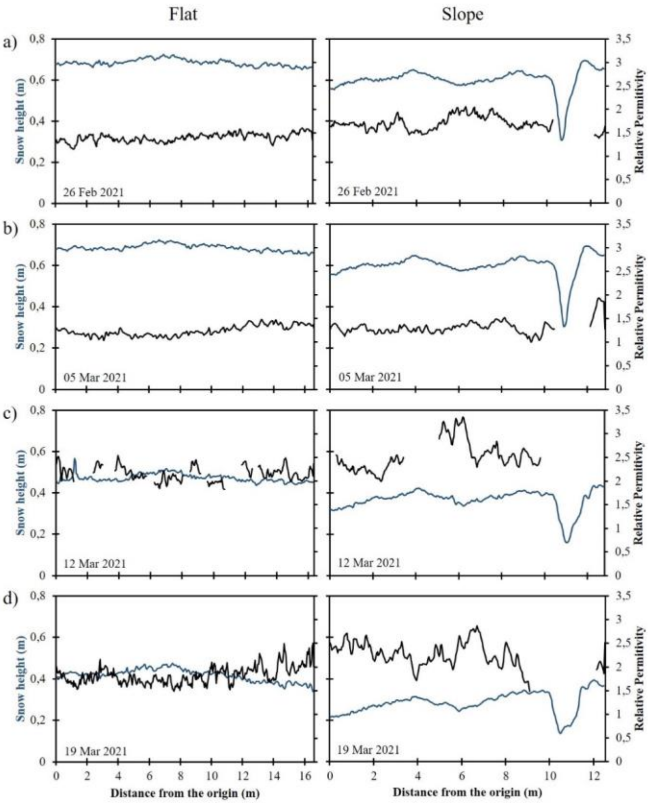

Figure 6~~5~~: Bulk permittivity (black line) and snow depth (blue line) calculated for the flat (left) and slope (right) transects on: a) February 26; b)March 5; c) March 12 and d) March 19.~~Bulk permittivity and snow depth calculated for the flat and slope transects on February 26, March 5, March 12 and March 19.~~ Adapted from Valence and Baraer (2021).

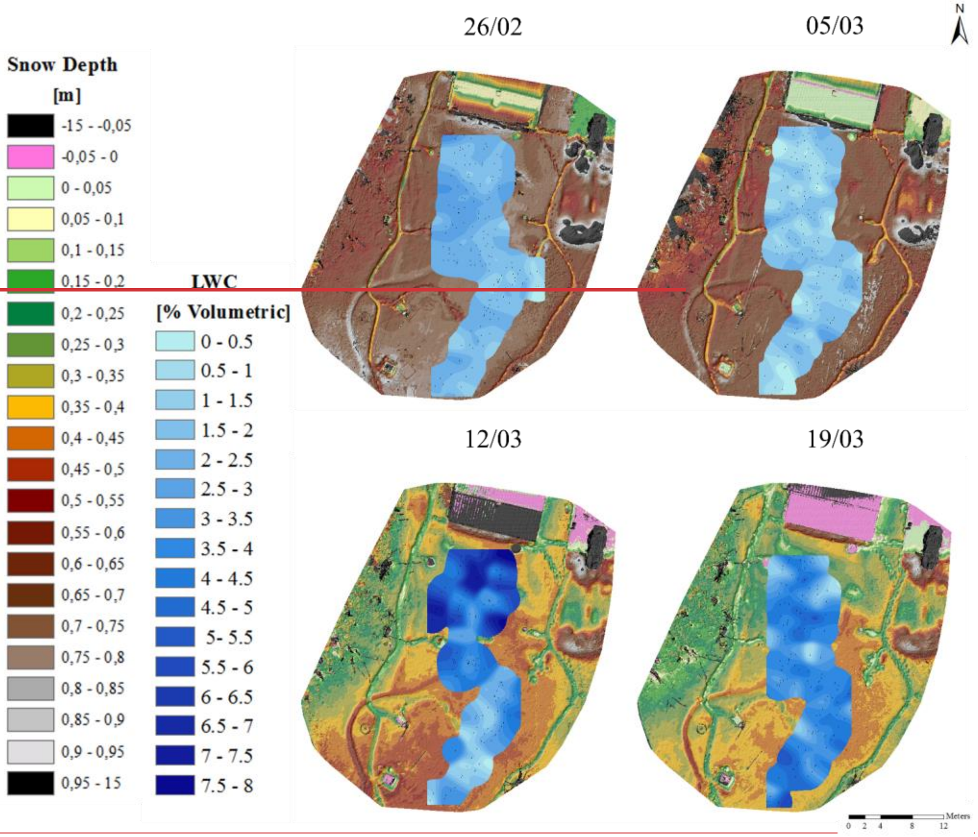
26/02
05/03
12/03
19/03
N
Snow Depth
[m]
-15 - -0,05
-0,05 - 0
0 - 0,05
0,05 - 0,1
0,1 - 0,15
0,15 - 0,2
0,2 - 0,25
0,25 - 0,3
0,3 - 0,35
0,35 - 0,4
0,4 - 0,45
0,45 - 0,5
0,5 - 0,55
0,55 - 0,6
0,6 - 0,65
0,65 - 0,7
0,7 - 0,75
0,75 - 0,8
0,8 - 0,85
0,85 - 0,9
0,9 - 0,95
0,95 - 15
LWC
[% Volumetric]
0 - 0.5
0.5 - 1
1 - 1.5
1.5 - 2
2 - 2.5
2.5 - 3
3 - 3.5
3.5 - 4
4 - 4.5
4.5 - 5
5- 5.5
5.5 - 6
6 - 6.5
6.5 - 7
7 - 7.5
7.5 - 8
Meters
0 2 4 8 12

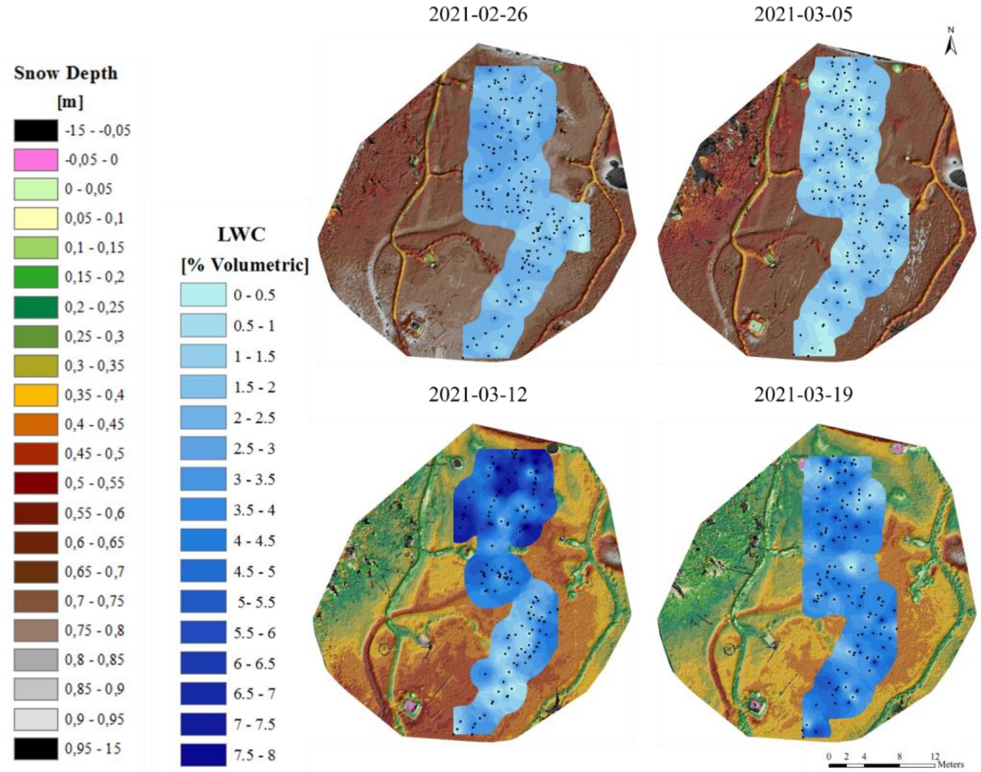

Figure 76: LWC calculated by GPR frequency dependent attenuation analysis. Points used for interpolation are displayed in black.

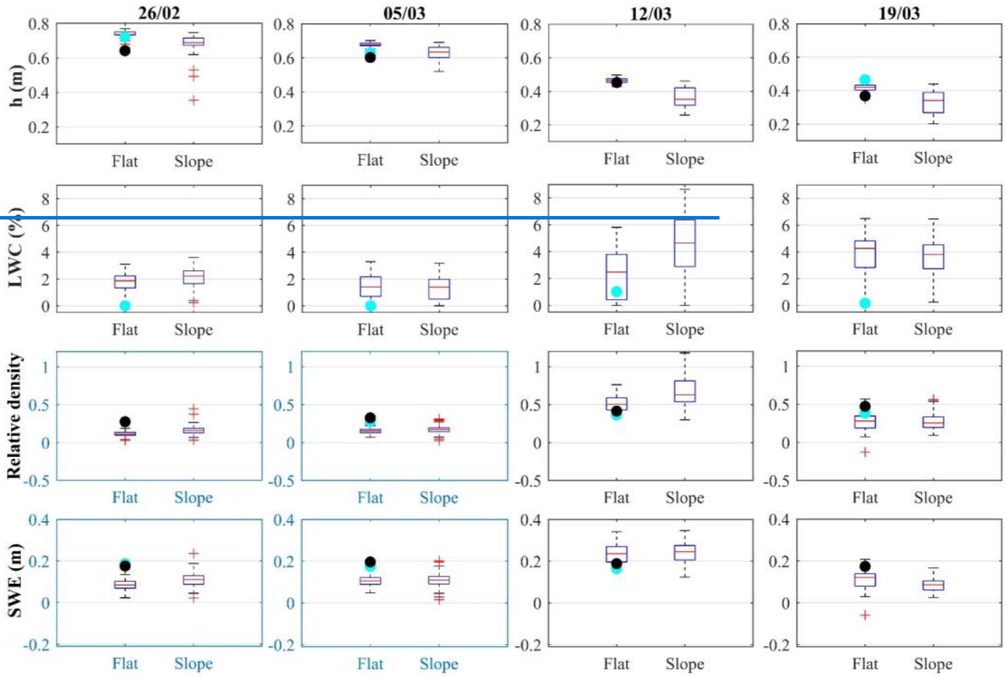

~~Figure 7: Box plots representing the snowpack studied variables for the sloped and flat areas for each survey date. In the boxes, the central red line represents the median, and the bottom and top blue edges mark the 25th and 75th percentiles, respectively. The whiskers show the data ranges excluding outliers. Wherever existing, outliers are represented by a red cross. Circle markers~~

~~represent reference values originating from the AWS (in blue) and snow pits (in black). Figures framed in blue were created with the assumption of a dry snowpack.~~

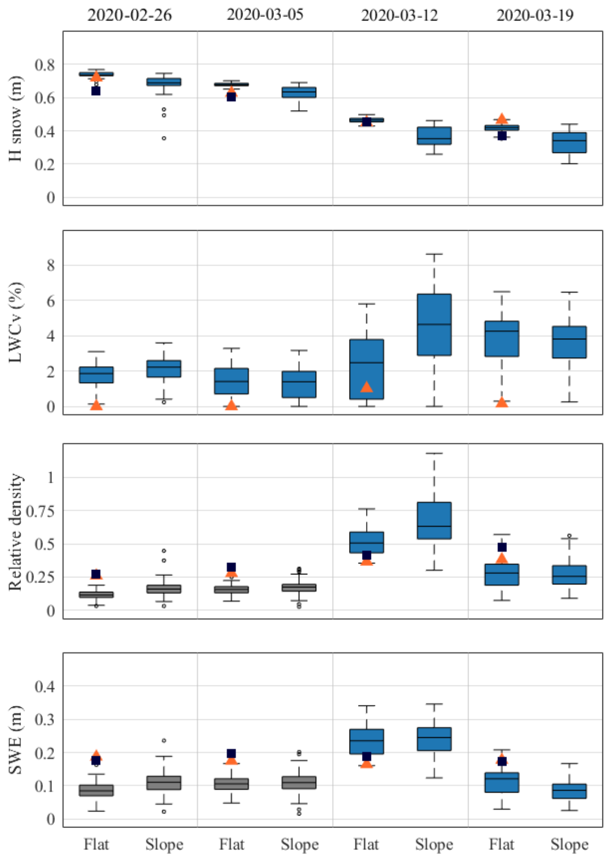

Figure 8: Box plots representing the snowpack studied variables for the sloped and flat areas for each survey date. In the boxes, the central black line represents the median, and the bottom and top edges mark the 25th and 75th percentiles, respectively. The whiskers show the data ranges excluding outliers. Wherever existing, outliers are represented by a black circle. Dark blue squared and orange triangles markers represent reference values originating from the AWS and snow pits, respectively. Grey boxes were created with the assumption of a dry snowpack.

1020

Table 1: List of the instruments used in this study. Accuracy is either given by the manufacturer or estimated for worst-case scenarios. Adapted from Paquotte and Baraer (2022).

Variable	Sensors	Manufacturer	Accuracy	Timestamp
T_{air}	Hygrovue10	Campbell Scientific	±0.6°C	15 min
Precipitation	Tipping Bucket Raingauge (52202)~~From P.E.T. station~~	Campbell Scientific	±3~~4.5~~%	15 min
Snow depth~~h~~	Ultrasonic (SR50A)	Campbell Scientific	±1 cm	15 min
$T_{n,cm}$	Thermal profiler (CS230)	Campbell Scientific	±0.2°C	15 min
Outflow	Lysimeter	Homemade	±1%	15 min
SWE	SWE sensor (CS725)	Campbell Scientific	±15 mm	6 h
Permittivity (ε)	TDR (CS610)	Campbell Scientific	±5%	15 min

Table 2: Methods combined in this study classified based on the sampling frequency and the spatial coverage.

Variable	Continuous, single point	~~Repetitive~~Repeated, single point	Repetitive, two surfaces
h	Sonic sensor	Snow pit	Photogrammetry
ρ	h / SWE	Snow pit	GPR
SWE	SWE sensor	Snow pit	GPR
LWC	TDR (2 points, 4 layers)	A2	GPR